Journal of Catalysis 454 (2026) 116637

Contents lists available at ScienceDirect

Journal of Catalysis

journal homepage: www.elsevier.com/locate/jcat

Research article

New bi-functional catalysts for a novel continuous production of propylene oxide with in-situ generated hydrogen peroxide

Christoph Schmidt [a], Matias Alvear [a], Francesco Sandri [a], Seo Mandon [a,b], Satu Ojala [c], Tiina Laitinen [c], Mika Lastusaari [d], Ilari Angervo [e], Tapio Salmi [a,f,*]

[a] Laboratory of Industrial Chemistry and Reaction Engineering (TKR), Åbo Akademi University, FI-20500 Turku-Åbo, Finland
[b] École des métiers de l'environnement, UniLaSalle Rennes, FR-35170 Bruz, France
[c] Environmental and Chemical Engineering, University of Oulu FI-90014 Oulu, Finland
[d] Intelligent Materials Chemistry Group, University of Turku FI-20014 Turku, Finland
[e] Wihuri Physical Laboratory, University of Turku FI-20014 Turku, Finland
[f] Department of Chemical Sciences, Università di Napoli "Federico II", IT-80125 Napoli, Italy

ARTICLE INFO

Keywords:
Epoxidation
One-pot reaction
Bi-functional catalysts
Titanium silicalite
Gold-palladium catalysts
Propylene oxide
Hydrogen peroxide

ABSTRACT

Combined direct synthesis of hydrogen peroxide (DSHP) and epoxidation of propene to propylene oxide with hydrogen peroxide (HPPO) was carried out first time in a continuous laboratory-scale trickle bed reactor operating under mild conditions of 8 bar and 10°C. The reaction was performed with bimetallic gold–palladium catalysts supported on titanium silicalite 1 (TS-1). Three series of catalysts were synthesized from two different lots of TS-1 and different calcination heating rates. The catalysts were extensively examined using XRD, SEM-EDS, TEM-SAED, STEM-EDS, ICP-OES, XPS, UV–vis DRS, nitrogen-physisorption and ammonia-TPD. The metal-modification of TS-1 containing anatase impurities was shown first time, where the preferential deposition site for the bimetallic nanoparticles was on the minor anatase phase, found in different amounts in commercial TS-1 materials. In the first catalyst series, a higher anatase content was found, which led to a decrease of the AuPd nanoparticle size compared to the second and third series. Increasing the heating rate in calcination resulted in an additional reduction of the AuPd nanoparticle size. The propylene oxide selectivity was 55.7 % using catalysts of the third series, while the propylene oxide production rate was 0.17 $mol \cdot kg_{cat}^{-1} \cdot h^{-1}$ with 19.2 % propene conversion. The use of a palladium-poor alloy was found to be crucial for this reaction system to limit the hydrogenation of hydrogen peroxide and propene. The catalyst activity was investigated in the separate processes of DSHP and epoxidation to get a deeper insight into the reaction mechanism. In the switch experiments, DSHP followed by the combined reaction of DSHP and HPPO, the competing side reactions, hydrogenation of propene and hydrogen peroxide were confirmed. In another experiment, the dismutation of hydrogen peroxide was disproved.

1. Introduction

Hydrogen peroxide (H_2O_2) is considered as an environmental-friendly oxidant due to its harmless degradation to water while possessing strong oxidation properties [1]. These features make H_2O_2 an excellent oxidant, which is used in several applications, particularly as a bleaching agent in pulp and paper and textile industries [2]. Furthermore, H_2O_2 is used in the chemical industry as a powerful oxidizer, for instance in the production of epoxides, caprolactam, sodium percarbonate, peracetic acids and other compounds [3,4]. Currently, the indirect anthraquinone process covers the demand of H_2O_2, despite its numerous drawbacks concerning side reactions, accumulation of impurities in the working solution and catalyst deactivation [4]. Consequently, large-scale production is required to maintain the process profitable.

An alternative reaction route is the direct synthesis of hydrogen peroxide (DSHP) from hydrogen and oxygen, which displays an environmentally-friendly process considering the atom efficiency of 100 % as well as the avoidance of toxic waste [5]. Moreover, the major advantages of DSHP are the straightforward process setup and the

* Corresponding author at: Laboratory of Industrial Chemistry and Reaction Engineering (TKR), Åbo Akademi University, FI-20500 Turku-Åbo, Finland.
E-mail address: tapio.salmi@abo.fi (T. Salmi).

https://doi.org/10.1016/j.jcat.2025.116637
Received 17 July 2025; Received in revised form 21 November 2025; Accepted 11 December 2025
Available online 13 December 2025

production of H_2O_2 in MeOH or MeOH/water solution, which can be used directly in subsequent reactions, while the distillation of H_2O_2 from the working solution is the critical issue of the anthraquinone process [6]. The main challenge with DSHP is that the process needs to be operated in a high dilution, as hydrogen and oxygen can form an explosive gas mixture. Another issue is the selectivity, as water is the favored product in DSHP [7]. Nevertheless, the principal simplicity of the process allows the DSHP to be linked to existing processes on site or combine them directly to a one-pot reaction and thus suppress the degeneration of H_2O_2. By combining with other processes, for example the production of methanol or benzyl alcohol, expensive purification steps can be omitted [8,9]. Other positive aspects of DSHP are the avoidance of the transportation of H_2O_2 from the production site to the user site and the synthesis from inexpensive oxygen and abundant hydrogen [10]. Current trends in the increasing use of electrolysis to produce hydrogen and oxygen as the co-product and the expansion of the hydrogen network favor the circumstances for DSHP.

In previous research, the preparation of various catalysts for the DSHP has been reported, which differ in metal composition, preparation method and support material [11–14]. The most frequently used active phase is Pd or an alloy of Pd, Au or Pt in different compositions [15]. It has been found that AuPd alloys are the most active binary species for hydrogen peroxide production, as Pd activates hydrogen while gold greatly reduces the O-O cleavage of Pd surfaces, which decreases water formation [16,17]. The metal can be introduced on a broad range of support materials, such as carbon, ion-exchange resins, alumina, silica, zirconia, ceria, titania, or zeolites [18–20]. The research on the epoxidation of olefins has been focused on zeolites as well, more precisely titanosilicates. Taramasso et al. published in 1983 a revolutionary report of titanosilicate-1 (TS-1), a zeolite which is able to activate H_2O_2 due to its tetrahedral coordinated Ti species in the MFI structure [21]. The titanium silicate is applicable for many oxidation processes, for example ammoxidation, oxidation of alcohols and epoxidation of alkenes [22–24].

Alternative synthesis routes have been discovered to produce highly valuable chemicals such as propene oxide (PO), which is one of the most crucial building blocks nowadays with a market volume of 21 billion USD in 2023 [25]. The chlorohydrin process is the traditional production route for PO but it has lost importance due to the stoichiometric production of a salt waste and the use of highly toxic and corrosive chlorine [26]. Nowadays, only 30 % of PO is produced by the chlorohydrin process [25]. Other important processes are the styrene monomer propylene oxide (SMPO) process and the *tert*-butyl alcohol (TBA) process, where PO appears as a stoichiometric co-product. The direct oxidation of propene with oxygen, catalyzed by noble metals, is of minor importance, suffering from low turnover frequencies and biochemical approaches are problematic owing to the stability of the organisms due to the toxicity of PO [27]. Overall, the trend is shifted to the environmentally friendly hydrogen peroxide to propylene oxide (HPPO) process, which covers about 20 % of the PO production nowadays. This process is still under investigation and intensification, so that various Ti containing catalyst materials have been screened, e.g. Ti-*Beta*, Ti-MOR, Ti-MCM, Ti-MWW [28]. Co-solvents have been used to improve the selectivity and kinetic studies have been carried out to gain a deeper understanding on the reaction mechanism [29,30].

Despite all the developments of HPPO, the disadvantage of this process is still the high cost of H_2O_2. However, in 1998, Hayashi et al. discovered that Au/TiO_2 can perform the epoxidation of propene in the presence of hydrogen and oxygen in the gas phase, opening the possibility of epoxidation with *in-situ* generated H_2O_2, achieving a PO selectivity exceeding 90 % with 1–2 % of propene conversion [31]. Many research groups have improved this procedure, for example, by using bimetallic catalysts [20], whose synergetic effects have been confirmed in the DSHP, due to the suppression of the H_2O_2 decomposition on the highly active Pd sites and oxygen activation on Au sites, resulting in an improvement of the H_2O_2 selectivity. Nevertheless, previous investigations have proven that the Pd sites in the AuPd alloy promote the propene hydrogenation [32]. According to our best knowledge, the highest production rate of PO in the one-pot reaction has been reported by Feng et al. to be 205 g $kg_{cat}^{-1} \cdot h^{-1}$ using Au/TS-1 in the gas phase at 200°C [33]. In other publications, it has been demonstrated that the epoxidation of propene with *in-situ* generated H_2O_2 can be performed in supercritical CO_2 or in plasma [34,35]. However, these operations require a high-energy input and temperatures of 100–200°C or supercritical CO_2, making them less attractive for industrial applications.

Thus, the aim of this work was the development of a process that operates continuously and under mild conditions in liquid phase in the same way as the separate DSHP and HPPO processes. Therefore, a heterogeneous catalyst with co-existing active sites is necessary, consisting of DSHP active AuPd nanoparticles and HPPO active Ti-zeolite, which can perform the combined reaction systems, sketched in Fig. 1. These catalysts were prepared, characterized and tested in a laboratory-scale trickle bed reactor to correlate their physico-chemical properties with their performance in the one-pot reaction, further called hydrogen to propylene oxide process (HyPO). Thanks to further catalytic studies in the separate processes, the dynamics of HyPO were unraveled.

2. Materials and methods

2.1. Materials

AuPd-TS1 catalysts were synthesized with commercial titanium silicalite 1 (TS-1) (ACS Materials), hydrogen tetrachloroaurate(III) trihydrate (Thermo Fisher scientific, 99.99 %), palladium chloride (Alfa Aesar, 99.9 %), urea (Sigma-Alrich, 99.5 %), hydrochloric acid (Sigma-Alrich, $\geq$ 37 %), ammonium hydroxide (Emplura, 32 %) and deionized water. For the chloride ion test, silver nitrate (Sigma-Alrich, 99.0 %) was used. Nitric acid (Fisher Scientific, 70 %) was used for passivation of the reactor system. In the catalytic experiments, quartz wool (Roth), glass wool (Merck) and quartz sand (Supelco) were used as packing materials for the reactor tube. The reactants, hydrogen (Woikoski, customized mixture of 4.89 % hydrogen in CO_2), oxygen (Woikoski, 99.999 %) and propene (Linde, 99.5 %) were dissolved in methanol (Sigma-Alrich, $\geq$ 99.9 %) while carbon dioxide (Woikoski, 99.995 %) was used as the inert gas and for pressurizing the reactor. Argon (Woikoski, 99.999 %) was used for pressure regulation. Propylene oxide (Sigma-Aldrich, 99.9 %) was used for calibration. In the epoxidation experiments, hydrogen peroxide (Sigma-Alrich, 30 % w/w) was mixed with methanol. Titanium (IV) oxysulfate (Sigma-Aldrich, 27–31 % sulfuric acid solution) was used for the analysis of hydrogen peroxide. The Karl-Fischer-titration was carried out with the titrant Hydranal™Composite 2 and Hydranal™Methanol dry (Honeywell/Fluka) of the water analysis.

2.2. Catalyst preparation

Co-precipitation with urea was used to introduce the metal onto the support material. In a typical catalyst synthesis experiment, $PdCl_2$ (6.67 mg) was dissolved with a few droplets of concentrated HCl and deionized water (200 ml) was added, after which $HAuCl_4 \cdot 3H_2O$ (71.01 mg) was added to the solution. The pH of the precursor solution was increased with 32 % NH_4OH to 2 or 2.5, depending on the catalyst batch, that the urea hydrolysis was able to reach pH 5.8 – 7.3. Urea (1 g) and TS-1 (7.96 g) were added to the flask. The pH was measured after each step, and the flask was covered with aluminum foil. The slurry was stirred vigorously at 250 rpm for 30 min at room temperature, heated at 80°C for 15 h and cooled down for 2 h under intensive stirring. The slurry was filtered and washed at first with 32 % NH_4OH and subsequently with deionized water until the chloride ion test was negative. The solid was dried 24 h at 60°C statically in a rotary evaporator under vacuum. In the last step, the as-synthesized catalyst was split into three equal parts, which were calcined at 300°C with the heating rates of 1.5,

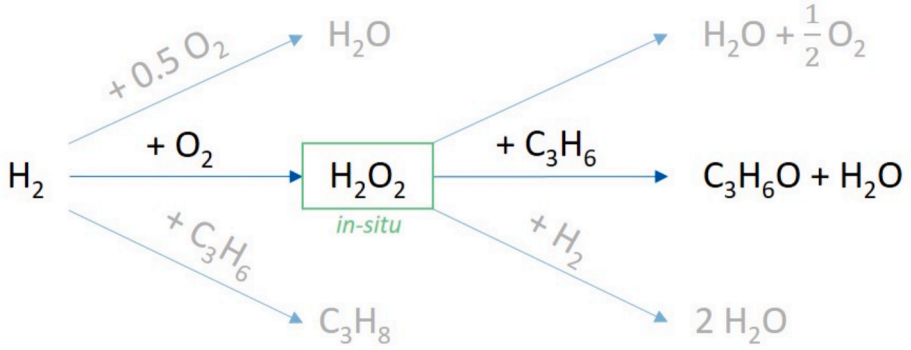

Fig. 1. Reaction scheme of combined DSHP and HPPO with side reactions.

5 or 10°C/min. The prepared catalysts are listed in the Table 1. The catalyst nomenclature includes the alloy type, TS-1 (TS1), calcination heating rate and the number of the synthesis batch.

2.3. Catalyst characterization

The crystallinity was investigated by powder X-ray diffraction (XRD) using a PANalytical Empyrean diffractometer with five axis goniometers. The incident beam optics consisted of Bragg-Brentano HD X-ray mirror, fixed 1/4° divergence slit, 10 mm mask, 0.04 rad soller slit and 1° antiscatter slit. The diffracted beam optics consisted of a 7.5 mm divergence slit, 0.04 rad soller slit and PIXcel detector array. The X-ray tube used was Empyrean Cu LFF. The X-ray radiation was filtered to include the Cu $K_{\alpha1}$ and Cu $K_{\alpha2}$ components only. The results were analyzed with MAUD (Material Analysis Using Diffraction) software [36]. Instrumental broadening was evaluated with Si standard samples. The results were obtained with 2θ scan range from 5° to 120°.

The morphology studies were conducted by using scanning electron microscopy (SEM) with energy dispersive X-ray spectroscopy (SEM-EDS) (Zeiss Leo Gemini 1530 with Thermo Scientific UltraDry silicon drift detector) and transmission electron microscopy (TEM) (JEOL JEM-1400Plus). For the TEM examination, the samples were dispersed in ethanol and sonicated before mounting on the grids. The particle sizes were determined with the software ImageJ. Additional structural studies were performed with transmission electron microscopy (TEM) (JEOL JEM-2200FS) coupled with selected area electron diffraction (TEM-SAED) for the crystal structure studies and scanning transmission electron microscopy with energy dispersive X-ray spectroscopy (STEM-EDS) for the element mapping.

The elemental analysis of the bulk material was performed with inductively coupled plasma – optical emission spectrometry (ICP-OES) (Agilent 5110 ICP-OES). The absorbance of silicon, aluminum and titanium was measured with radiation sources at wavelengths 288.2, 396.2 and 334.9 nm, respectively. The elemental compositions were calculated using the calibration curves generated from standard solutions. The oxidation states of Au, Pd, Ti and carbon were determined by using X-ray photoelectron spectroscopy (XPS) (Thermo Fisher Scientific ESCALAB 250Xi) equipped with a monochromatic Al K_{α} (1486.6 eV) radiation source and pass energy of 20 eV. The data were processed with the Thermo Avantage software and binding energies (BE) were referred to the C 1 s peak line at 284.8 eV. The coordination of the titanium species of the support material was investigated via diffuse reflectance UV–vis (UV–vis DRS). The reflectance spectra were measured with an Avantes Avaspec HS-TEC CCD spectrometer through an Avantes FC-UV600-1-SR fiber optic cable with an Avantes AvaLight-DHc employing deuterium and halogen lamps as light sources and an Edinburgh Instruments $BaSO_4$ disc as the white reference. The absorbance was calculated from the reflection spectra according to the Kubelka-Munk theory. The signal was processed with the Savitzky-Golay smoothing algorithm with a window size of 10 and were normalized to [0,1].

The specific surface area and porosity were determined by nitrogen physisorption (Micrometrics 3Flex-3500) using the Dubinin-Radushkevich method for calculating the specific surface area and density functional theory (DFT) for the determination of the pore volume and pore size distribution. Before the measurements, the samples underwent *ex-situ* degassing at 0.1 mbar and 180°C for 24 h. The acidity of the materials was measured by temperature programmed desorption (TPD) (Microtrac Belcat II) equipped with a quartz tube reactor and a thermal conductivity detector (TCD), using ammonia as the probe molecule. The samples were pretreated at 300°C with a rate of 10°C/min and keeping the temperature for 60 min under He flow (30 ml/min). The ammonia absorption was performed at 100°C with a gas mixture of 7.5 % NH_3/He for 30 min (30 ml/min). The sample was flushed with He for 60 min and cooled down to 50°C. The ammonia desorption was analysed up to 800°C, with a heating rate of 10°C/min, under a 30 ml/min He flow. The target temperature was kept for 20 min. The surface charge properties of the TS-1 materials were investigated with zeta potential analysis (Malvern Zetasizer Nano-ZS) combined with an automatic titrator (Malvern MPT-2). For the measurements, 10 mg of the material was dispersed in 10 ml deionized water and sonicated. The analysis was stabilized at pH 7 and conducted towards pH 1.5.

Table 1
Synthesis of AuPd catalysts with different TS-1 lots and varying calcination conditions.

Catalyst name	TS-1	Synthesis batch	Calcination conditions
AuPd-TS1-1.5-1	1st Lot	1st Batch	300°C, 3 h, 1.5°C/min
AuPd-TS1-5-1	1st Lot	1st Batch	300°C, 3 h, 5°C/min
AuPd-TS1-10-1	1st Lot	1st Batch	300°C, 3 h, 10°C/min
AuPd-TS1-1.5-2	2nd Lot	2nd Batch	300°C, 3 h, 1.5°C/min
AuPd-TS1-5-2	2nd Lot	2nd Batch	300°C, 3 h, 5°C/min
AuPd-TS1-10-2	2nd Lot	2nd Batch	300°C, 3 h, 10°C/min
AuPd-TS1-1.5-3	2nd Lot	3rd Batch	300°C, 3 h, 1.5°C/min
AuPd-TS1-5-3	2nd Lot	3rd Batch	300°C, 3 h, 5°C/min
AuPd-TS1-10-3	2nd Lot	3rd Batch	300°C, 3 h, 10°C/min

2.4. Experimental setup for catalytic experiments

The catalytic experiments were performed in a co-current trickle bed reactor (TBR) made of AISI 316 stainless steel, 30 cm long and with I.D. 12 mm, as is illustrated in Fig. 2. A copper coil encircled the reactor and allowed temperature control from −20°C to 100°C by an external thermostat (Grant LT D6G). Calibrated mass flow controllers (MFC) (Brooks 5866 and 5850 series) were implemented to set the gas flow rates. Methanol was used as the liquid phase and fed with a high-pressure liquid metering pump (Eldex ReciPro Series 2000). A thermocouple monitored the temperature inside of the reactor tube. The reactor was equipped with a rupture disk as safety measure. The pressure was regulated by a backpressure controller (BPC) (U3L Ultra Low Flow Back Pressure Regulator) installed at the tubular reactor. After the

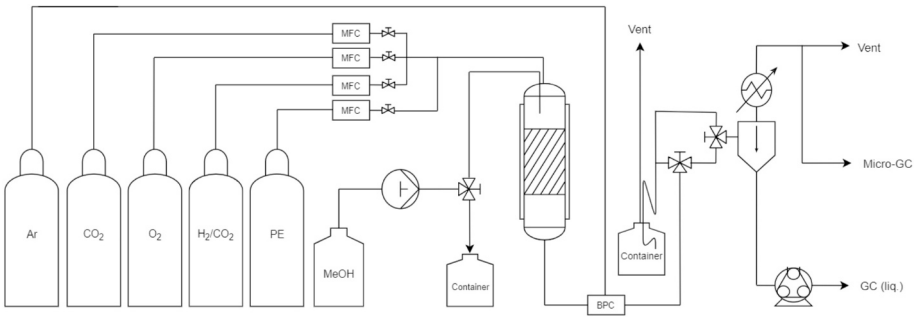

Fig. 2. Experimental setup for the epoxidation of propene (MFC = mass flow controller, BPC = backpressure controller, GC = gas chromatograph).

backpressure controller, a sample line and a "night line" for overnight experiments were implemented. In the sample line, the gas and liquid phases were separated in a three neck-round flask with a condenser set to −5°C on top for recovering volatile compounds. The liquid was sampled from the round flask with a pump (Heidolph Pumpdrive 5206). In the "night line", the gas and liquid phases were continuously separated by a double siphon, so that the liquid was collected in a bottle and the gas flow steadily passed the three-neck-round flask and allowed the online-analysis with the micro gas chromatograph (*Micro*-GC).

The micro-GC (Agilent 490 MicroGC) used for gas analysis was equipped with a thermal conductivity detector (TCD). Four capillary columns (10 m MS 5A, 6 m 5CB, 10 m Al_2O_3/KCl, and 10 m PPU) separated the gas mixture at 80°C and with helium as the carrier gas, except for the molecular sieve column at 100°C and with nitrogen as carrier gas. The liquid samples were analyzed with a gas chromatograph (GC) (Agilent 6890 N G1540N) equipped with a capillary column (Plot U). The column, with a length of 60 m, a diameter of 530 µm and an active phase thickness of 20 µm, was operated at 185°C. The gases were calibrated with a one-point calibration by sampling 10 times a gas mixture containing hydrogen (4.27 vol %), oxygen (4.17 vol %), propene (8.49 vol %), and CO_2 (83.13 vol %). The response factor of propane was assumed to be equal to that of propene since a TCD was used and the thermal conductivities of both gases differ just about 0.0015 Wm^{-1} K^{-1} [37]. The calibration of the GC for propylene oxide was conducted with 0.01; 0.025; 0.05; 0.075; 0.1; 0.15 and 1 wt % solutions in methanol.

For the H_2O_2 analysis, the liquid sample was weighted and 0.5 ml of titanium oxysulfate solution was added. The yellow complex formed was diluted with water to 10 ml and the absorbance at 409 nm was measured with a UV–vis spectrometer (Shimadzu UV-2600i). A solution with 2 ml methanol, 0.5 ml titanium oxysulfate filled up to 10 ml with water was used as the reference in the double beam device [38]. The calibration of the method was done by measuring the absorbance of 0.0047; 0.0093; 0.0187; 0.0467; 0.093; 0.187; 0.467; 0.933 and 1.87 mM H_2O_2/methanol solutions. The water analysis was conducted via Karl-Fischer titration with a titrator (Metrohm 736 GP Titrino). Before the analysis, the device was daily calibrated three times with an injection of 10 µl water to determine the response factor. The methanol, used as the liquid phase for the reaction, was analysed three times with an injection of 0.5 ml to distinguish between water that had formed during the experiment.

2.5. Catalytic experiments

Hydrogen and oxygen can form explosive gas mixtures. The use of CO_2 as inert gas can reduce the flammability significantly and promotes the solubility of the other gases in the system [39]. For the sake of safety, H_2 was supplied as a ready mixture with CO_2 to always ensure the dilution with oxygen. Before the experiments, the reactor walls were passivated by filling up the volume four times with 30 % HNO_3 to prevent the decomposition of H_2O_2 [40]. The catalysts were pelletized and sieved to a fraction of 32– 63 µm for the experiments. The reactor was packed from bottom to top: glass wool, quartz sand (125–250 µm), quartz wool, catalyst layer, quartz wool and quartz sand (125–250 µm). For the catalyst layer, 1 g of catalyst was diluted in 20 g of quartz sand (<125 µm) to improve the heat transfer and the H_2O_2 selectivity [41]. The first sand layer kept the catalyst layer in the middle of the reactor between quartz wool, while the second layer ensured the mass transfer of the gases into the liquid.

The experiment started with pressurizing the reactor with CO_2 to 8 bar and cooling the reactor at 10°C. After the pressure and temperature had stabilized, the methanol flow (1 ml/min) was turned on. After the first methanol droplet passed the outlet, the catalyst bed was wetted for 1 h. Finally, the reaction started by switching from CO_2 to the reactant gas mixture. The gas and liquid flow rates were selected to operate in the trickle-flow regime [42]. The typical reactant gas mixture for HyPO consisted of 0.14 mmol/min of propene (PE), 0.07 mmol/min of O_2, 0.07 mmol/min of H_2 and 1.46 mmol/min of CO_2 with a total volumetric flow rate of 40 ml/min at atmospheric pressure. The ratio of the gases were changed for the DSHP, HPPO, H_2O_2 decomposition experiments and the hydrogenation/oxidation of PE, while the total gas flow rate was kept at 40 ml/min by substituting the missing fraction with CO_2, e.g. for HPPO the molar flow of CO_2 was 1.60 mmol/min and PE 0.14 mmol/min. The liquid phase for the HPPO and dismutation experiment consisted of 0.0165 mmol/ml H_2O_2 in methanol, confirmed by UV–vis analysis. To shut down the reactor system, the reactant gas mixture was switched to only CO_2, while keeping the pressure and cooling of the reactor. After 30 min flushing CO_2, the methanol flow and reactor cooling were turned off. After 1 h, the reactor tube was depressurized to atmospheric pressure and the CO_2 gas flow was turned off. In the case of consecutive experiments, the reactor with the catalyst inside was kept in the setup after the shutting down procedure and the following experiment was started as previously described. The reactions were continuously monitored by taking liquid samples to obtain information from the transient and stationary states. The gas samples were withdrawn automatically online by the micro-GC.

The conversions of hydrogen, oxygen and propene were calculated as follows,

$$X(\%) = \frac{\dot{n}_{\text{in}} - \dot{n}_{\text{out}}}{\dot{n}_{\text{in}}} \times 100 \quad (1)$$

where the subscripts *in* and *out* denote the inlet and outlet molar flows of hydrogen, oxygen or propene. Since no ring opening products were observed in the experiments, the selectivity of propylene oxide (PO) was defined as

$$S(\%) = \frac{\dot{n}_{\text{PO}}}{\dot{n}_{\text{PO}} + \dot{n}_{\text{propane}}} \times 100 \quad (2)$$

Another indicator used is the hydrogen efficiency (HE),

$$HE(\%) = \frac{\dot{n}_{\text{PO}} + \dot{n}_{H_2O_2}}{\dot{n}_{H_{2_{in}}} - \dot{n}_{H_{2_{out}}}} \times 100 \quad (3)$$

to determine the conversion of hydrogen to the desired product (PO) and the intermediate product (H_2O_2).

3. Results and discussion

3.1. Catalyst synthesis

The initial approach to obtain a suitable catalyst for HyPO was to combine the different active sites of the DSHP and HPPO processes. The most active bimetallic alloy for the DSHP is AuPd with a metal composition of 80 % gold and 20 % palladium, which activates hydrogen with Pd but inhibit over oxidation to H_2O due to the presence of gold [43]. In a preliminary test of HyPO, a catalyst with this metal composition on TS-1 formed excessively propane as the Pd catalyzes all hydrogenation reactions in HyPO and its content is still too high for a selective hydrogenation. Thus, it was decided to prepare catalysts with a palladium content as low as 10 % in the AuPd alloy to further inhibit the hydrogenation ability, increasing the H_2O_2 selectivity and suppressing propane formation. In the HPPO process, TS-1 is the most used catalyst and commercially available. However, the deposition of gold on the titanium silicates has been challenging but with deposition precipitation satisfying results have been achieved [44]. In this work, the urea deposition precipitation method was chosen due to its applicability on a broad range of different oxide supports resulting in high-dispersed gold nanoparticles particularly after long synthesis times [45]. The applicability of the method for bimetallic systems has been demonstrated for AuPd/TiO_2 [46]. To guarantee an even deposition of Pd with Au, $PdCl_2$ was chosen as the precursor forms after addition of HCl H_2PdCl_4, being similar to the $HAuCl_4$ complex. A washing step with NH_4OH was introduced to fix the nanoparticles to the support after the synthesis, before washing with water [47]. In the first deposition attempt, the urea hydrolysis could not neutralize the very acidic slurry and the metal precursors remained in solution. Therefore, the pH was increased from 0.8 to 2.5 with 32 % NH_4OH, so that the urea hydrolysis initialize the precipitation. In fact, it is known that the addition of ammonium increases the surface charge of TS-1 and therefore improves the attraction of negative charged metal precursors [48]. The urea deposition of the first batch (AuPd-TS1-x-1) with prior NH_4OH adjustment succeeded and the pH reached 6.5 (Table 2). In case of the second batch (AuPd-TS1-x-2), the precursor solution became cloudy after increasing the pH from 1.5 to 2.5, indicating a premature precipitation. The addition of less NH_4OH to reach pH 2.5, probably did not sufficiently reduce the negative surface change of TS-1, discussed in Section 3.2. The pH increase in the third batch (AuPd-TS1-x-3) was limited to 2, preventing premature precipitation. Since the starting pH was lower than in the first batch catalyst, the final pH of 5.8 was 0.7 lower compared to the first batch. Due to the inappropriate metal deposition in the second synthesis, proven by TEM (S 1), the catalysts AuPd-TS1-x-2 were not further characterized.

3.2. Catalyst characterization

The findings of the crystallinity analysis had the most prominent influence on other catalyst properties and consequences on the catalytic performance. Initially, the titanium silicate crystal structure of the commercial materials was intended to be confirmed using XRD. In Fig. 3, the XRD pattern of the AuPd catalysts of the first and third series as well as the pure TS-1 materials are displayed.

All the materials showed as their main phase the characteristic reflections at $2\Theta = 7.9°$, $8.7°$, $23.0°$, $23.7°$ and $23.4°$ of the MFI structure, which is consistent with the simulated TS-1 pattern. However, a reflection of the anatase phase was found at $25.3°$, and only for the first series catalysts also at $37°$, $37.8°$ and $38.6°$ [49]. The occurrence of the anatase phase originates from the hydrothermal synthesis of titanium silicate, in which not all of the Ti is incorporated into the MFI framework and titania is formed from excess Ti during the crystallization process [50]. Thereby, the intensity of the anatase reflections decreases dramatically when comparing the first series with the third one. The intensity of the anatase reflection remained the same after the catalyst synthesis compared to the starting material used in the respective lot. From the reference intensity ratio (RIR), it was calculated that the first lot TS-1 contains 7.93 vol % of anatase while the second lot, used for the third catalyst series, contains 0.33 vol % of anatase. Reflections from the metal were not found due to the low loading and small size of the nanoparticles.

For the further determination of the different phases, SEM micrographs were recorded. In Fig. 4, TS-1 of the first lot is imaged, and the different morphologies are clearly visible. The majority of particles were present as cauliflower-like spheres. Besides them, cubic and elliptic particles were found in smaller amounts. Thereby, the spheres possess diameters between 155 – 440 nm, the cube an edge length of 85–310 nm and the ellipsoids have a maximum feret diameter of 150–440 nm. According to the previously discussed XRD results, it can be assumed that the cubic and elliptic particles represent the anatase phase, since they are present in a smaller amount than the cauliflower-like particles.

To obtain information about the compositions of the different particles, SEM-EDS of single particles were performed. The results of the analyzed particles of Fig. 5 are displayed in Table 3 and in S 3. Hereby, two different methods were applied, measuring either a single spot or a small area. Both results confirmed a significant difference in the elemental composition, where cubic particles have a Ti content of 10.4–17.3 at %, whereas the spherical particles contain 2.2–3.9 at % titanium or the titanium signal in the spectrum was too weak to be detected. The titanium-rich composition of the cubes is a strong indication of the presence of TiO_2, but the atomic percentages need to be used with caution since the X-ray beam can interfere with underlying particles, leading to small errors in the measurement.

In the back-scattered electron (BSE) images, the contrast between heavy and light atoms is well visible. Therefore, the Ti-rich cubes and ellipsoids were displayed brighter than the Si-rich spheres in the unmodified support material (Fig. 6a), indicating cubes to be anatase. Moreover, the BSE images were used to study the distribution of metal particles. To our surprise, the different particle morphologies play a crucial role in the deposition. It was found that the cubes and ellipsoids were fully decorated with AuPd nanoparticles (Fig. 6b, red frames) while the spheres were nearly unmodified (Fig. 6b, light blue frame). The material of the cubes and ellipsoids likely exert a stronger attraction during the metal deposition. Besides the metal-decorated cubes and ellipsoids, metal aggregates were also found in the BSE images as big bright spots (Figs. 6c and 6d, light green frame). The formation can be caused by oversaturated sites of the cubes and ellipsoids and is more stable in aggregates than onto the spherical particles. Interestingly, the aggregation level was lower for catalysts of the first series, which is logical considering the higher content of anatase in the first lot TS-1 and consequently, a higher metal uptake capacity.

For a more detailed investigation of the deposition pattern and the determination of the size of the supported metal nanoparticles, TEM analysis was conducted. The micrographs displayed in Fig. 7 are representative for all the catalysts of the first (7a, 7b) and third series

Table 2
Synthesis batches of AuPd catalysts with varying pH.

Catalyst	Amount	[Au] + [Pd] + HCl *pH*	+NH_4OH *pH*	+ TS-1 *pH*	+Urea *pH*	+15 h *pH*
AuPd-TS1-x-1	8 g	0.8	2.5	2.5	2.6	6.5
AuPd-TS1-x-2	10 g	1.5	2.5	2.6	2.6	7.3
AuPd-TS1-x-3	10 g	0.5	2.0	2.0	2.1	5.8

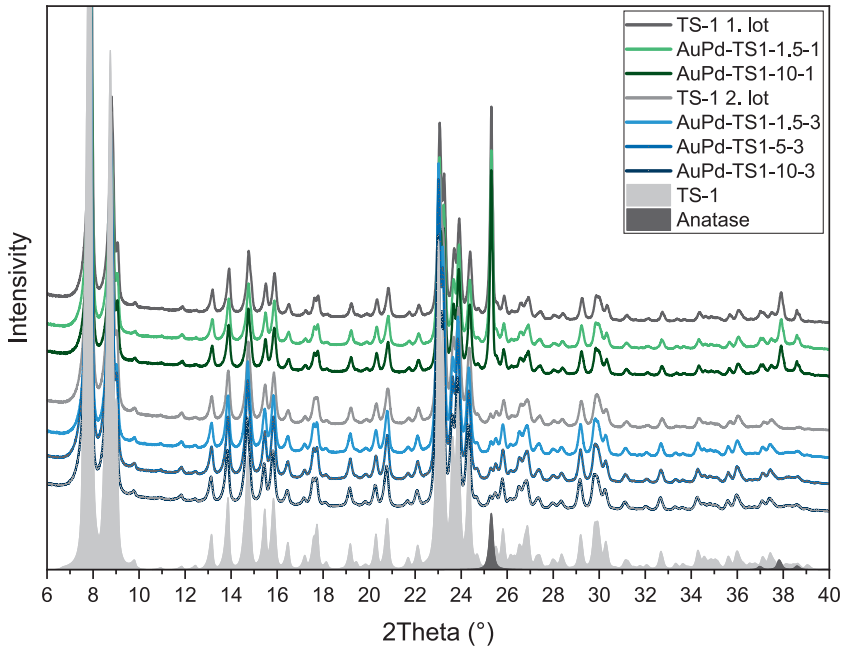

Fig. 3. XRD pattern of different TS-1 materials and synthesized AuPd-TS1 catalysts of the first and third series. The filled grey and dark grey patterns are simulated reflections of TS-1 (ICSD 93539) and anatase (ICSD 121632).

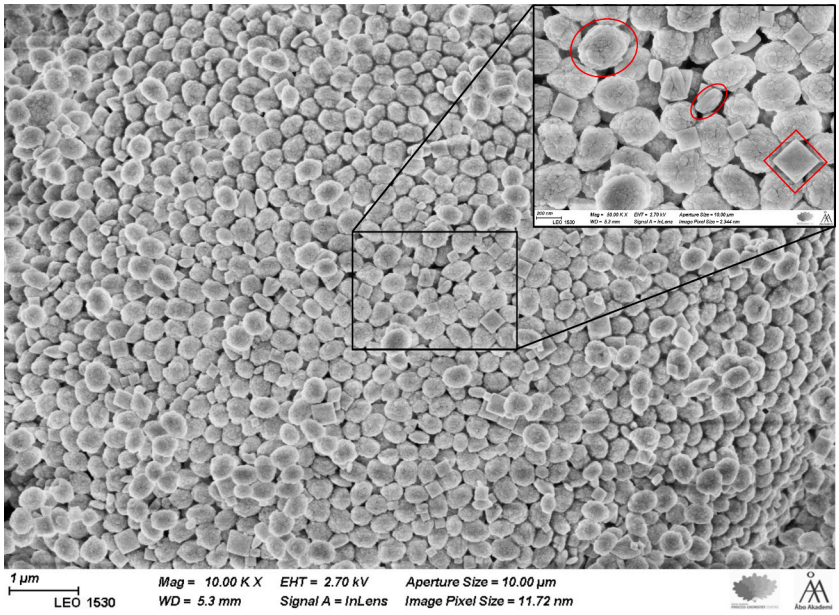

Fig. 4. Scanning electron micrograph of TS-1 of the first lot with its different morphologies.

(7c, 7d). The deposition pattern, which was already found in the BSE images, is present in the samples, where a small amount of metal particles was supported onto the spherical support particles while the cubic and oval support particles were covered with metal particles. This pattern was found independently of the different calcination procedures. The examination of an uncalcined catalyst using TEM, shown in S 2, confirms an uneven deposition before the calcination. Consequently, the selective deposition takes place in the metal impregnation step, due to stronger interaction of the metal precursors and the cubic and elliptical particles.

TEM-SAED was the only analytical method that was able to identify the actual nature of the three particle morphologies. In all diffraction patterns, displayed in Fig. 8, a spot diffraction pattern was obtained showing that all particles are present as single crystals. From the d-spacing of the spots in Figs. 8d and 8e, the *hkl* indexes were determined and distinctly assigned to the tetragonal anatase phase for cubes and ellipsoids. The measured d-spacings of the TS-1 SAED pattern, reported in S 4, slightly differ from literature as the substituted titanium distorts the orthorhombic MFI lattice [51]. Nevertheless, the cauliflower-shaped spheres can be assigned to the titanium silicate phase considering the distortion. It can be concluded that the metal deposition occurs preferentially to the anatase phase as both cubes and ellipsoids are identified as the anatase phase.

The preferential deposition of the metals on titania is confirmed by the zeta potential of TS-1, as this material is negatively charged at pH 1.5 (Fig. 9). In contrast, anatase is positively charged at pH lower than 3 or

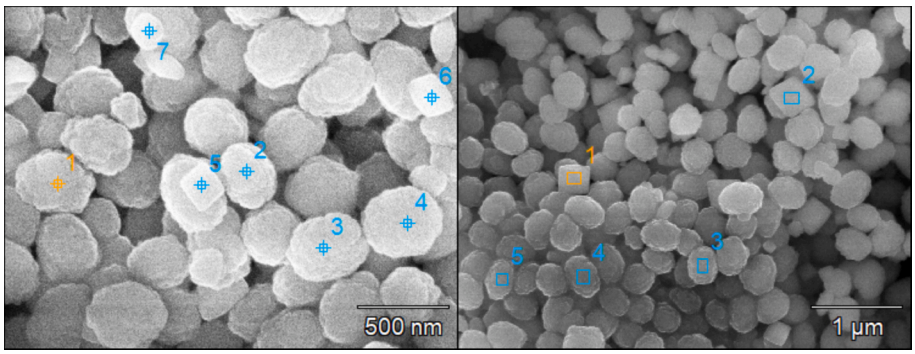

Fig. 5. Punctual (left) and areal (right) EDS on scanning electron micrographs of TS-1.

Table 3
Results of EDS-SEM (Fig. 5) of the oxides in at%. The results of the cubic particles are marked in blue.

Measurement	Punctual		Measurement	Areal	
	Si	Ti		Si	Ti
1.	28.9	–	1.	13.6	13.9
2.	30.5	–	2.	10.1	17.3
3.	29.3	–	3.	31.3	–
4.	25.0	3.9	4.	27.6	3.4
5.	18.8	10.4	5.	27.4	2.2
6.	15.7	11.3			
7.	25.4	3.2			

5, depending on the Ti precursor [52]. Due to the different isoelectric points (IEP), the negative charged metal precursors are preferentially adsorbed onto less negatively charged titania instead of TS-1. The influence of anatase in the support materials on the zeta potential was found, when comparing the first lot TS-1 with a higher surface charge in the pH range from 1.5 to 7 than the second TS-1 lot, due to the higher anatase content. Another reason for the preferential metal deposition on anatase could be the presence of defects in the titanium oxide structure, which attract metal precursors [53].

The effect of a stronger metal-support interaction on anatase is reflected in the size distribution of the metal nanoparticles, which is narrower and nearly half-sized than the distribution on titanium silicalite (Fig. 10), indicating the sintering of the weaker bounded particles during the calcination process (Table 4). Therefore, it was decided to report the nanoparticle size distribution of metal particles on anatase and TS-1 separately.

In Table 4, the influence of the different calcination heating rates on the mean particle size is reported. A trend is noticed in which the mean size of AuPd particles on TS-1 and anatase decreases slightly from the lowest to highest heating rate for both catalyst series. AuPd particles became smaller by 0.26 nm in the first series and 0.42 nm in the third series on anatase, and on TS-1 1.3 nm in the first series. A simple explanation can be that the particles are exposed to heat for a longer time at the lower heating rates, until the final temperature is reached. Thus, the metal atoms are mobile for a longer time, promoting sintering.

STEM-EDS, was used to determine the chemical composition of the nanoparticles and the support material. In Fig. 11 and S 5, the element mapping of Si, Ti, Pd and Au of fresh AuPd-TS1-10–3 is displayed. These images are representative for all the catalysts. The most striking feature

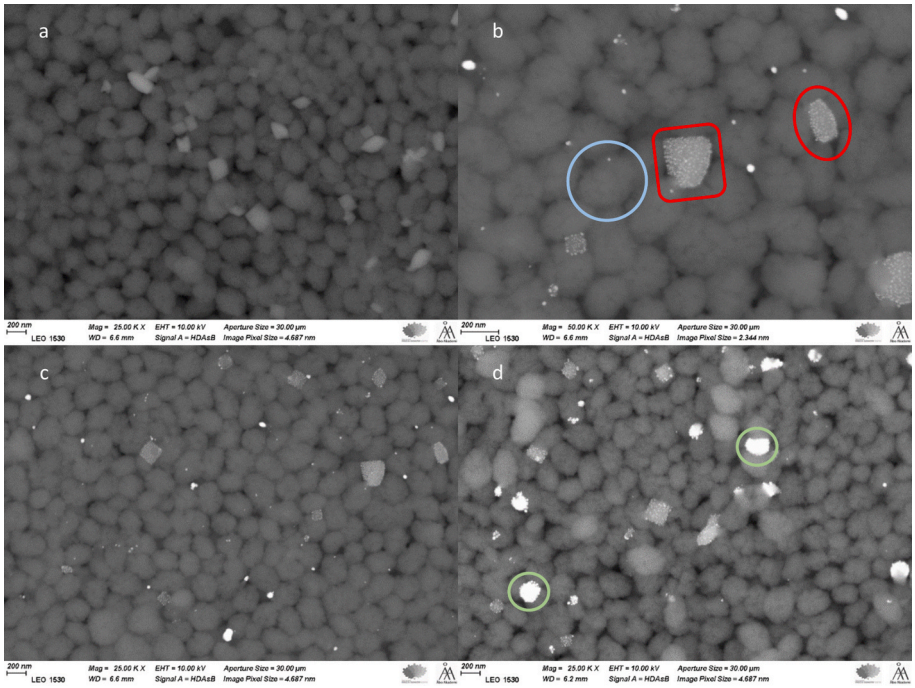

Fig. 6. Back-scattered electron images of a) TS-1, b) and c) AuPd-TS1-10–1 with metal decorated cubes and ellipsoids (red frames) and nearly unmodified spheres (light blue frame), and d) AuPd-TS1-10–3 with metal aggregates (light green frames). (For interpretation of the references to colour in this figure legend, the reader is referred to the web version of this article.)

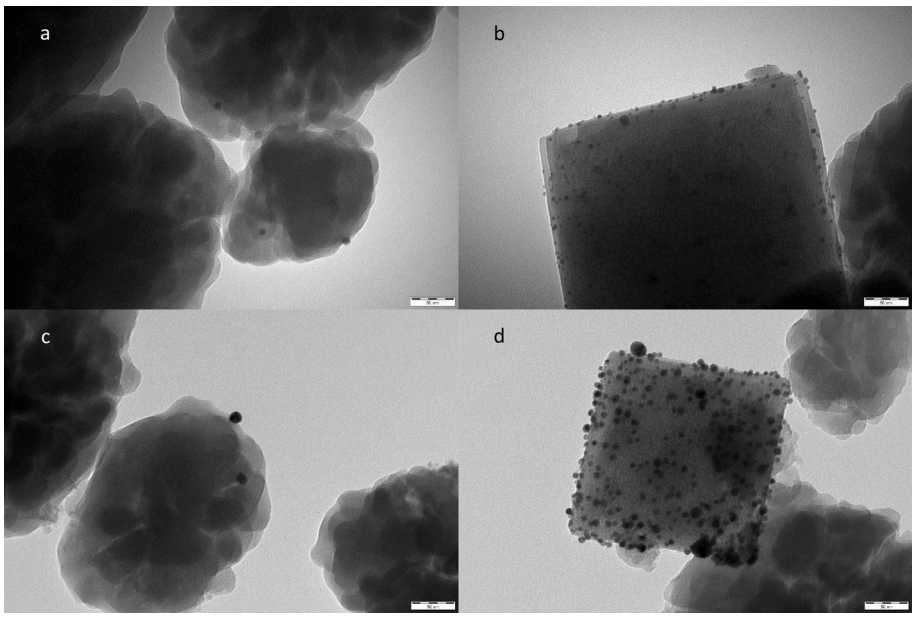

Fig. 7. Transmission electron micrograph (TEM) of AuPd-TS1-10–1 (a, b) and AuPd-TS1-10–3 (c, d) with AuPd nanoparticle on titanium silicalite (left) and anatase (right) particles.

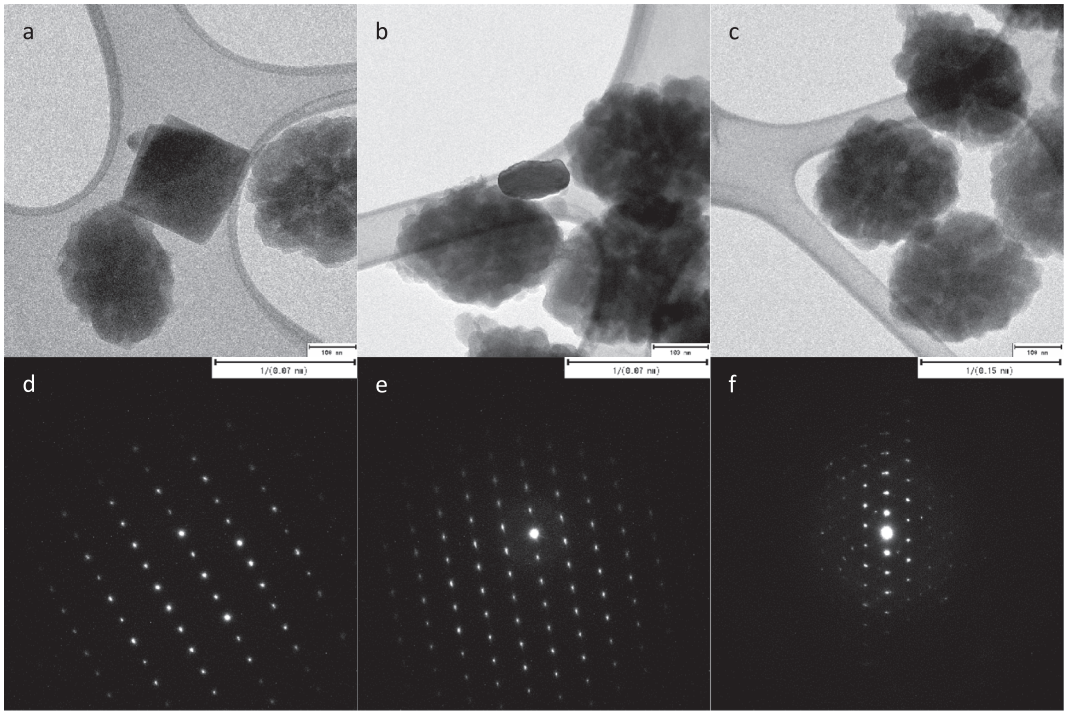

Fig. 8. Transmission electron micrographs of cubic (a) and elliptic anatase (b), and TS-1 (c). The corresponding SAED-patterns are shown in d, e, f of the upper transmission electron micrograph.

in the various maps is that the support particles contain either Si or Ti in high concentrations, revealing the different chemical compositions of TS-1 and anatase. The findings confirm the TEM-SAED results, where the cubes and ellipsoids are identified as anatase, while titanium silicate is assigned to the spheres. A further finding from the element mapping is that Au and Pd appear at the same locations, as seen in Figs. 11e and 11f. A rise of the Pd concentration profile in the line scans can be also observed when the Au concentration profile increases, indicating an alloy of both metals.

The measurement of small particles was challenging, however, particles larger than 20 nm could be measured. Since the specific spectral signals of Pd and Au partially overlap with those of Ti and Si, the metal appears to be evenly distributed over the support particles. However, the even metal distribution is ostensible as it originates from the interferences of Si and Ti signals. Only visible metal in the original STEM images coincide with the accumulated spots in the EDS maps of Pd and Au. Nevertheless, the element mapping and line scan results prove the bimetallic character of the nanoparticles and the applicability of the urea co-precipitation to synthesize AuPd alloys.

To determine the chemical composition of the bulk materials, ICP-

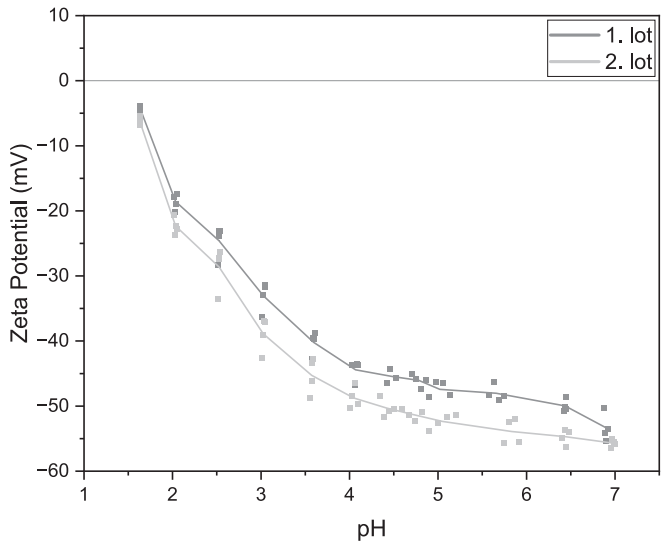

Fig. 9. Zeta potential measurements of the first and second lot of the TS-1 materials.

OES measurements were carried out. The element analysis revealed a uniform metal loading and composition among the different batches (Table 4). This result was expected for each series, as the catalysts originate from the same synthesis batch, but also between the two catalyst series the metal loading difference was minor. The actual loading 0.36–0.40 wt % for the first and third series deviate from the nominal loading 0.5 wt %. A reason for the loss of metal might be the first washing step with ammonium hydroxide, which is intended to fix the nanoparticles to the support material during calcination, but weaker bounded metal ions can be removed by a harsh chemical treatment [47]. Regarding the nominal loading of Pd and Au, the percentage loss of palladium was 52 %−54 % higher compared to gold with a loss of 16 %−25 %. Consequently, the AuPd alloy had a palladium content of 6.3–6.5 % in the first catalysts series and 5.7 %–6.0 % in the third instead of the aimed Pd content of 10 %. The framework Ti content of 1.2 at % in the support material was specified by the supplier. The low Ti concentration in the TS-1 particles is visible from the element mapping, where titanium is almost exclusively present in cubes and ellipsoids, as the framework single atoms are not visible in the mapping.

In the XPS spectra, shown in Fig. 12, palladium can be found as metallic Pd^0. For fresh AuPd-TS1-10-3, the Pd $3d_{3/2}$ peak is observed at 340.3 eV and for fresh AuPd-TS1-10-1 at 339.9 eV. The Pd $3d_{5/2}$ peak is overlapping with the gold Au $4d_{5/2}$ peak [54]. Gold is present in the oxidation states of the metallic form Au^0 and, exclusively in AuPd-TS1-10-1, partially reduced gold precursor Au^{1+}. The Au $4f_{7/2}$ peak is observed at 83.7 eV for fresh AuPd-TS1-10-1 corresponding to Au^0, and 0.7 eV lower than for AuPd-TS1-10–3, indicating a stronger metal-support interaction. The shift to a lower BE was also observed for Pd with 0.4 eV difference. The BE shifts likely due to a charge transfer from the anatase to gold and increase of the electron density in the metal particle [55]. In AuPd-TS1-10–1, 28 % of gold is present as Au^{1+} calculated from the Au $4f_{7/2}$ peak areas. For fresh AuPd-TS1-10–3, Au $4f_{7/2}$ peak is observed at 84.0 eV, which is reported for bulk gold [56]. This observation is consistent with the results presented in Fig. 6, where more unsupported metal aggregates were found in AuPd-TS1-10–3. In the Ti spectra of fresh AuPd-TS1-10–1, two Ti species can be found corresponding to framework Ti at 460.4 eV and 466.5 eV and the extra-framework Ti of anatase at 458.7 eV and 464.4 eV [57]. The shifted Ti $2p_{3/2}$ peak at 460.4 eV indicates the interaction between Ti and Si [58]. The Ti peaks of anatase were not detected in the spectra of fresh AuPd-TS1-10–3, consistent with the low anatase content found in the XRD analysis. The difference between the fresh and spent catalysts is discussed in the catalyst deactivation section 3.4.

The different coordinated Ti-species were identified with DRS UV–vis. In the spectra of the catalytic materials, shown in Fig. 13, three titanium specific absorption bands of tetrahedral, tetrapodal (210 nm), tetrahedral, tripodal (235 nm) and extra-framework (330 nm) Ti-species were observed [59].

The bands of tetrapodal and tripodal tetrahedral Ti were strongly overlapped, making the quantification difficult. The absorbance of the extra-framework titanium, which can be assigned to anatase, significantly declines from the first lot TS-1 to the second lot. These results are

Table 4
Mean size of AuPd nanoparticles on different sites, and metal loading and composition of different catalysts.

Catalyst	AuPd nanoparticle size on anatase [nm]	AuPd nanoparticle size on TS-1 [nm]	Metal loading (Au/Pd) [wt%]
AuPd-TS1-1.5-1	4.91 ± 0.24	8.99 ± 0.28	0.365 (0.342/0.024)
AuPd-TS1-5-1	4.75 ± 0.14	8.1 ± 0.3	0.363 (0.339/0.023)
AuPd-TS1-10-1	4.65 ± 0.08	7.7 ± 0.3	0.366 (0.343/0.023)
AuPd-TS1-1.5-3	8.52 ± 0.12	14.3 ± 0.6	0.383 (0.360/0.023)
AuPd-TS1-5-3	8.38 ± 0.12	12.2 ± 0.4	0.382 (0.359/0.022)
AuPd-TS1-10-3	8.10 ± 0.10	13.6 ± 0.5	0.398 (0.375/0.023)

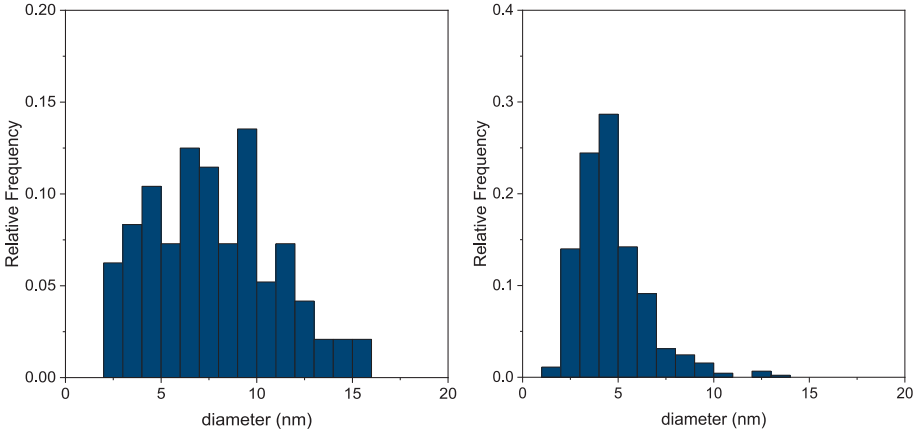

Fig. 10. Nanoparticle size distribution of AuPd nanoparticles on TS-1 (left) and anatase (right) support particles (AuPd-TS1-10–1).

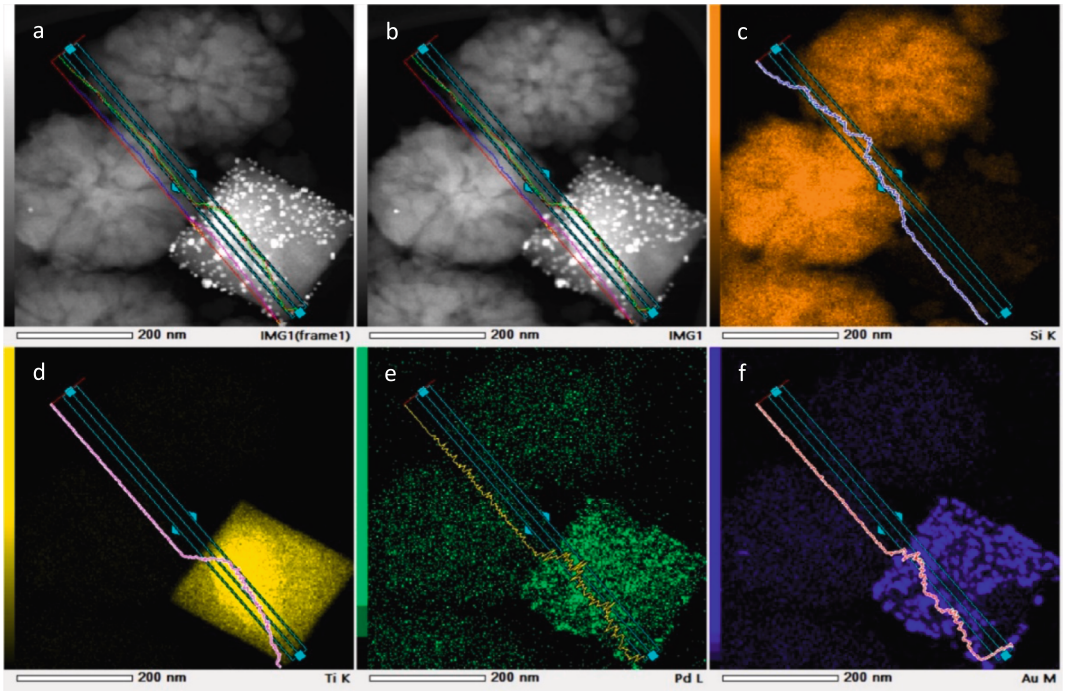

Fig. 11. STEM-EDS with line scans of fresh AuPd-TS1-10–3; a) and b) STEM image, c) Si, d) Ti, e) Pd and f) Au.

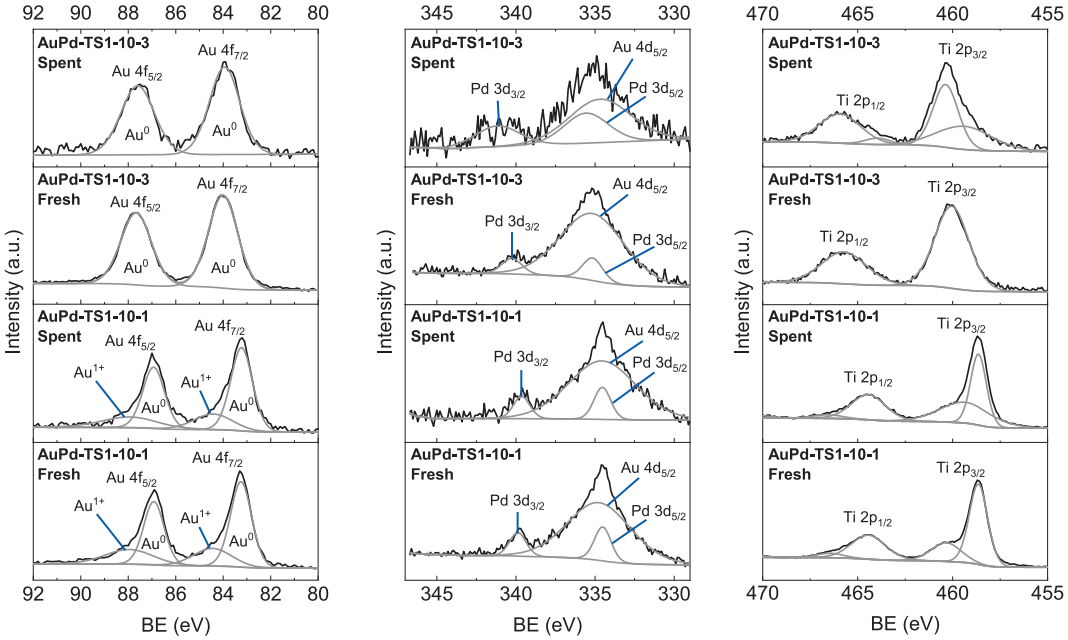

Fig. 12. Gold (Au 4f), Pd (Pd 3d) and Ti (Ti 2p) XPS spectra of AuPd-TS1-10–1 and AuPd-TS1-10–3 before and after usage in HyPO.

consistent with the XRD results, where a bigger fraction of anatase was found in the first lot of TS-1. The metal modified materials show similar spectra with respect to the TS-1 lot, which had been used for the catalyst synthesis, confirming that the metal deposition does not affect the topology of the support materials. In addition, a weak surface plasmon resonance (SPR) band of the gold alloy was found in the metal-modified samples of the third series at 500 – 600 nm, as Pd damp it intensity [60].

From the investigation of the textural properties via nitrogen physisorption, it was found that all the catalysts within the series have similar specific surface areas (SSA) and pore volumes, as reported in Table 5. Only AuPd-TS1-5-3 showed a lower SSA (348 m^2/g) compared with AuPd-TS1-1.5-3 and AuPd-TS1-10–3 with 459 m^2/g and 453 m^2/g, respectively, and differed in the isotherms (S 6). The catalyst AuPd-TS1-1.5-1 and AuPd-TS1-10-1 have with 395 m^2/g and 396 m^2/g a significant lower SSA, as the catalysts of the third series. The larger proportion of titanium silicate, which is known to have a high SSA due to the microchannel system, in the second TS-1 lot, can explain this observation. Indeed, the pore volume increased from 0.25–0.26 cm^3/g to 0.30 cm^3/g comparing the first to the third catalyst series, and the micropore volume increased by 0.04 cm^3/g from the first to third catalyst series. When comparing the catalyst batch with the pure support material which had been used, a decrease of the SSA was observed due to clogging of pores with AuPd particles after introduction of the metal [33]. The nitrogen physisorption experiments revealed that the pore structure

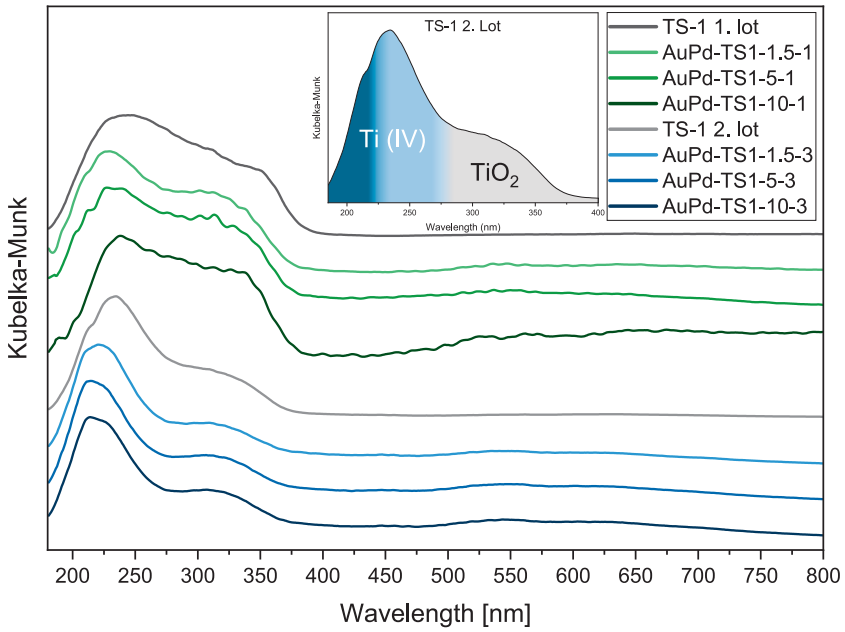

Fig. 13. DRS UV–vis spectra of AuPd-TS1 catalysts of the first and third series and the corresponding TS-1 lot. In the magnified spectra of TS-1 2. Lot, the band regions of tetrahedral coordinated Ti(IV) (tetrapodal in dark blue and tripodal in light blue), and extra-frame work Ti (TiO_2) (grey) are shown. (For interpretation of the references to colour in this figure legend, the reader is referred to the web version of this article.)

Table 5
The textural and chemical properties of AuPd-TS1 and TS-1 catalysts. SSA – specific surface area, V_{pores} – pore volume and d_{pores} – average pore width.

Catalyst	SSA[a] [m^2/g]	V_{pores}[b] [cm^3/g] V_{tot}	V_{micro}	d_{pores}[c] [nm]	Acidity[d] [μmol/g]
AuPd-TS1-1.5-1	395	0.250	0.192	0.61	27.6
AuPd-TS1-10-1	396	0.260	0.194	0.61	29.1
AuPd-TS1-1.5-3	459	0.307	0.228	0.61	24.9
AuPd-TS1-5-3	348	0.216	0.169	0.61	30.1
AuPd-TS1-10-3	453	0.302	0.228	0.62	23.2
TS-1 (1st Lot)	397	0.232	0.189	0.62	68.0
TS-1 (2nd Lot)	515	0.302	0.245	0.62	42.6

[a] Calculated with Dubinin-Radushkevich method.
[b] Calculated with Tarazona NLDFT method.
[c] Calculated with Horvath-Kawavoe method.
[d] Calculated with *Ammonia*-TPD.

was preserved after the metal deposition and aligns with the reported MFI structure (S 7) [61].

The acidity measurement via ammonia-TPD is shown in S 8. Two signals were observed at 95 – 105°C and 135 – 155°C, representing weak Lewis acid sites due to embedded Ti(IV) in TS-1 and anatase [62,63]. The signal around 100°C declined with a decreasing anatase content and therefore can be assigned to the Ti sites in anatase, resulting in a decrease of the overall acidity from 68.0 μmol/g to 42.6 μmol/g. After the metal modification of the support materials, a decline in the acidity is observed, decreasing to 27.6–29.1 μmol/g and to 23.2–30.1 μmol/g, to the catalyst of the first and third series, respectively. The decline of the acidity can be explained by the deposition of metal on the acid sites, and a higher metal dispersion blocks the Ti sites more effectively. AuPd-TS1-5-3 has a higher acidity (30.1 μmmol/g), which might be related to the findings of the loss of surface area observed.

3.3. Catalytic experiments in trickle bed reactor

To the best of our knowledge, combined continuous processes of DSHP and propene epoxidation in liquid phase have not been reported yet in open literature. The first step in this work was the development of catalysts, bearing AuPd nanoparticles for the DSHP step, enabled hydrogen and oxygen activation, and tetrahedral Ti sites for the consecutive HPPO step, facilitated the activation of the in-situ generated H_2O_2. In preliminary experiments with a $Au_{80}Pd_{20}$ catalyst, only traces of PO were detected, as propene and H_2O_2 hydrogenation dominated the reaction system. In contrast, the use of an $Au_{90}Pd_{10}$ alloy resulted in sufficient PO production and therefore defined the metal composition used for this study. A monometallic Au catalyst was inactive DSHP, confirming the essential role of Pd in the alloy for HyPO.

The second step in the development of the HyPO process involved the determination of appropriate reaction conditions necessary for a successful operation, as no comparative benchmarks are available for such a combined system. The investigation of various reaction conditions in the separated DSHP and HPPO processes using a trickle bed reactor has been described previously [42,64]. The two key parameters that differ the most are pressure and temperature. The DSHP has been carried out at −10°C to increase the gas solubility and to suppress H_2O_2 dismutation, and at 10 bar to enhance the gas–liquid mass transfer. On the other hand, in HPPO, the conversion of propene had an optimum at 40°C, but the selectivity of PO decreased at temperatures exceeding 25°C due to the formation of ring-opening products. Increasing the pressure in HPPO up to 4.5 bar gave an improved propene conversion, whereas only minor changes were observed at higher pressures. To find a good compromise between DSHP and HPPO, in which the formation of the ring-opening products and the H_2O_2 decomposition are minimized, it was decided to start the HyPO process at 20°C as the decomposition of H_2O_2 does not take place at such a low temperature. The DSHP requires a high pressure, but propene is liquefied at 10.2 bar and 20°C [65], so it was decided to operate the system at 9 bar to avoid the condensation of propene. The optimum gas and liquid flow rates were taken from the DSHP reference to achieve a sufficient H_2O_2 production rate, which is expected to be the limiting factor in HyPO, and to comply with the safety regime. In addition to the gases used in the DSHP, propene was added in excess related to H_2 and O_2 to shift the chemical equilibrium towards PO. The total gas and liquid flow rates were maintained the same as in the DSHP to operate within the trickle flow regime.

3.3.1. Pre-run DSHP

The first catalytic experiment gave already important insights into the reaction dynamics. Initially, the DSHP was to be operated first and the propene flow switched on after reaching the steady state in the DSHP. However, after 600 min, the H_2O_2 production rate was still increasing in the DSHP pre-run, displayed in S 9. At TOS = 600 min, 0.0695 mmol/min (99.9 %) of hydrogen and 0.0212 mmol/min (18.9 %) of oxygen were converted, while 0.0064 mmol/min H_2O_2 and 0.0965 mmol/min H_2O were produced. The high consumption of hydrogen compared to oxygen, as well as the formation of more H_2O than fed reactants, which could be explained by an oxidation of methanol to formaldehyde and water, and sequential hydrogenation to methanol. Methanol is also directly involved in the reaction mechanism and does not only act as the solvent [66]. However, the precise measurement of the formaldehyde content is difficult, as this intermediate might appear in low concentrations compared to methanol. A reaction with CO_2 can be neglected considering the high thermodynamic stability and the mild reaction conditions.

3.3.2. HyPO experiments with AuPd-TS1-x-1

To be able to carry out HyPO in the next experiment, all three reactants were introduced simultaneously to the reactor system from the beginning. In the first experiment, HyPO did not reach the steady state. Therefore, the reaction was restarted two more times, as shown in Fig. 14. In each experiment, the H_2O_2 production rate increased sharply after a start-up period and subsequently declined. After the decline, a slow increase in the H_2O_2 production rate to 0.0008, 0.0017 and 0.0025 mmol/min was recorded in the first, second and third experiment, respectively. Moreover, the H_2O_2 production started, after the spike, at the same level as at the end of the previous experiment, which means that the catalytic system is preserved even though the reaction was stopped and restarted between two successive experiments. The change of the reaction conditions after the second experiment did not affect this pattern.

The steady increase in the H_2O_2 production rate indicates a slow change of the catalytic system. Fig. 14 reveals that the PO production starts when the H_2O_2 production declines, demonstrating the consecutive character of the reaction of PO production from the in-situ formed H_2O_2. Evidently, the induction period of the epoxidation is due to the activation of the framework titanium in TS-1 with H_2O and H_2O_2, which changes its coordination and can be proven by the XPS results of the spent catalyst in Section 3.4. Despite the steadily increasing H_2O_2 production rate, the PO production rate remained stable at 0.007 mmol/min during the first experiment and even slightly declined to 0.006 mmol/min during the second and third experiment. For all the experiments, PO was produced in similar amounts, even though the reaction conditions were changed after the second experiment.

After the first two experiments, it was decided to decrease the temperature to hinder the propene hydrogenation and promote the DSHP, and the pressure was decreased to avoid propene condensation. Besides the changed reaction conditions between the first two experiments to the third one, the ratio of propane and propene can be compared and give an indication about the extent of propene hydrogenation. In S 10, the gas analysis shows that the molar flow of propane declined in the first experiment, whereas it became stable after three hours in the second experiment, confirming the very slow stabilization of the reaction system. Comparing the propane-to-propene ratio in the third experiment with the previous ones, the ratio was significantly lower, indicating suppressed propene hydrogenation at lower temperatures. Since the PO production rate was on the same level in all the experiments while the propane production rate was reduced in the third, HyPO is more efficient under these conditions. After 420 min TOS in the third experiment, hydrogen was converted to 94.2 %, oxygen 22.4 % and propene 45.5 %. Thereby, the PO selectivity was 15.7 % with a HE of 13.5 %. The hydrogen and oxygen consumptions in the three experiments were similar to the DSHP pre-run, however, 52 % of the converted hydrogen formed propane and the H_2O formation, 0.048 mmol/min at TOS = 300 min, was cut by half compared to the DSHP. The reduced H_2O formation, which also includes H_2O as a co-product of the epoxidation, indicates that the consecutive epoxidation with H_2O_2 competes with the H_2O_2 hydrogenation, which is described in more detail in the step experiment from DSHP to HyPO. In this experiment and all following experiments, no ring-opening products were detected, as the operating conditions are very mild for the HPPO process.

For the following catalytic experiments, a nightline was implemented in the setup to perform longer experiments. Surprisingly, the catalyst AuPd-TS1-5–1 in HyPO became inactive after 32 h, whereby all the reactant conversions declined to nearly 0 %, as reported in S 12. The examination of the spent catalyst revealed that AuPd nanoparticles aggregated, as seen in S 11, which can explain the tremendous decline of

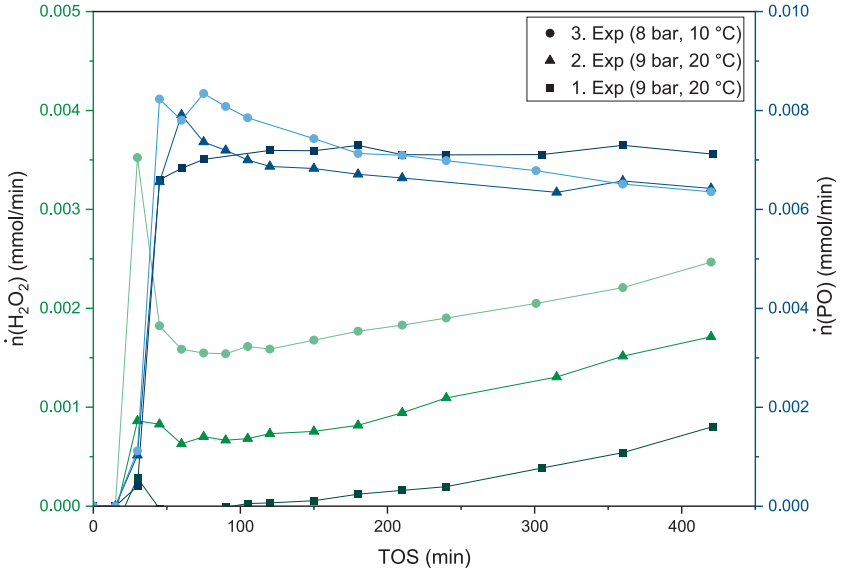

Fig. 14. Hydrogen peroxide (green) and PO (blue) production in HyPO for three experiments (1. square, 2. triangle and 3. circle) with AuPd-TS1-1.5–1. Reaction conditions: 0.07 mmol/min H_2, 0.11 mmol/min O_2, 0.13 mmol/min propene, 1.42 mmol/min CO_2; 9 bar, 20C (1. and 2. Exp) or 8 bar, 10C (3. Exp). (For interpretation of the references to colour in this figure legend, the reader is referred to the web version of this article.)

the catalyst activity. At this stage, according to the collected results, it was not possible to identify an explanation for such a strong deactivation, and more investigations are needed to describe this phenomenon.

The catalytic experiment with AuPd-TS1-10-1 in HyPO consisted of four individual runs since after the first run, lasting for 1920 min, the system did still not reach the steady state. After every run, the reactor was shut down and started up for the following one. In the gas (Fig. 15) and liquid analysis (Fig. 16), practically the same chemical composition was found after the re-start. Only from the third to the fourth run, a slightly higher decline in the H_2O_2 and PO production rates was observed. In the beginning of the fourth run, fine particles were flushed out from the reactor, due to a rapid de-pressurizing of the reactor after the third run, which damaged the pressed catalyst particles and explains the decrease of the catalytic activity in that specific run. In all the runs, particularly in the first and fourth run, the conversion of hydrogen and propene were declining, as seen in the gas analysis (Fig. 15). Despite the decrease of the consumed H_2, the H_2O_2 production rate was increasing (Fig. 16), which cannot be explained only with the decrease of the propane formation. This indicates a more efficient utilization of hydrogen, in which the hydrogenation of H_2O_2 is suppressed with an increasing TOS. Therefore, the conversion of propene to PO was stable being 0.0078 mmol/min in the first run and 0.0060 mmol/min in the fourth run with AuPd-TS1-10-1 (Fig. 16). Interestingly, the PO production rate increased steadily in the second and third run with AuPd-TS1-10-1, after it was relatively stable in the first run.

Noteworthy, the third run started on the following day, whereas between the first and second run, there was a break of nine days. A consideration is that during the break, a redox process with residues of MeOH inside the reactor could change the oxidation state of the metal particles to the initial state of the catalyst. It could also explain the decline in the H_2O_2 production rate and the higher conversion hydrogen compared to the end of the first run, due to restored catalyst properties. From the first to the third run with AuPd-TS1-10-1, the hydrogen efficiency (HE) improved steadily (Table 6), due to the higher production rate of H_2O_2 and PO while the hydrogen conversion declined. Interestingly, the more the catalyst was used, the more the reaction of hydrogen shifted from the formation of propane to desired products and improved the PO selectivity.

3.3.3. Step experiment DSHP to HyPO and ratio change of reactants

Another experiment was performed with AuPd-TS1-10–1, where the process was started with DSHP followed by HyPO to examine the H_2O_2 production rate and determine the efficiency of the H_2O_2 conversion into PO. In the third part of the experiment, the H_2:O_2:PE ratio was changed from 1:1:2 to 1:2:1 to increase the PO selectivity by suppressing the hydrogenation of propene and enhancing the production of H_2O_2. The results are summarized in Table 7. The H_2O_2 production rate increased over time during the DSHP as well as during the HyPO (Fig. 17). In the DSHP, an over consumption of H_2 (72.8 %) and O_2 (17.3 %) was noticed, excluding the part of reactants that formed H_2O_2. This means that about two times more H_2 was consumed than would be required for the H_2O formation. This reaction pattern of excessive H_2 consumption is similar to the DSHP pre-run with AuPd-TS1-1.5-1 and indicates once more the presence of another reaction that could not be identified. When switching from DSHP to HyPO, 58 % of the previously formed H_2O_2 is converted to PO at TOS = 1500 min, as shown in Fig. 17, and the sum of PO and H_2O_2 account only for 66 % of H_2O_2 before the switch. This finding, together with the reduced O_2 conversion indicates an overall lower production of H_2O_2 and shows a competing adsorption of propene on the active sites for DSHP. However, excluding the H_2 consumed in the PE hydrogenation, only 37.8 % of H_2 is converted meaning that the combustion or hydrogenation of H_2O_2 are significantly suppressed in the presence of the olefin. As in the HyPO with AuPd-TS1-10–1, the H_2O_2 production rate continuously increased despite the slight declining oxygen and hydrogen conversions (Table 7, S 13), indicating a more efficient utilization of the reactants and supporting the assumption that the combustion or hydrogenation of H_2O_2 are suppressed. Noteworthy, the catalytic system became more active in comparison with the previous experiment. At 1500 min TOS almost double the PO was produced than in the fourth run. An activation of Ti-species with H_2O_2 during the DSHP is a possible reason n[67]. In the last stage of the experiment, the H_2O_2 production rate was doubled after changing the ratio (Fig. 17), although the hydrogen feed remained the same, and the propene conversion to propane changed from 24.0 % to 26.6 %. However, the absolute propane production rate was suppressed by 23.8 % and therefore the PO selectivity increased from 22.6 % to 24.3 %, and the HE changed from 22.2 % to 26.3 %. The final PO production rate decreased to 16.2 % with the reactant ratio change. However, the process with the 1:2:1 H_2:O_2:PE gas ratio achieved a more efficient

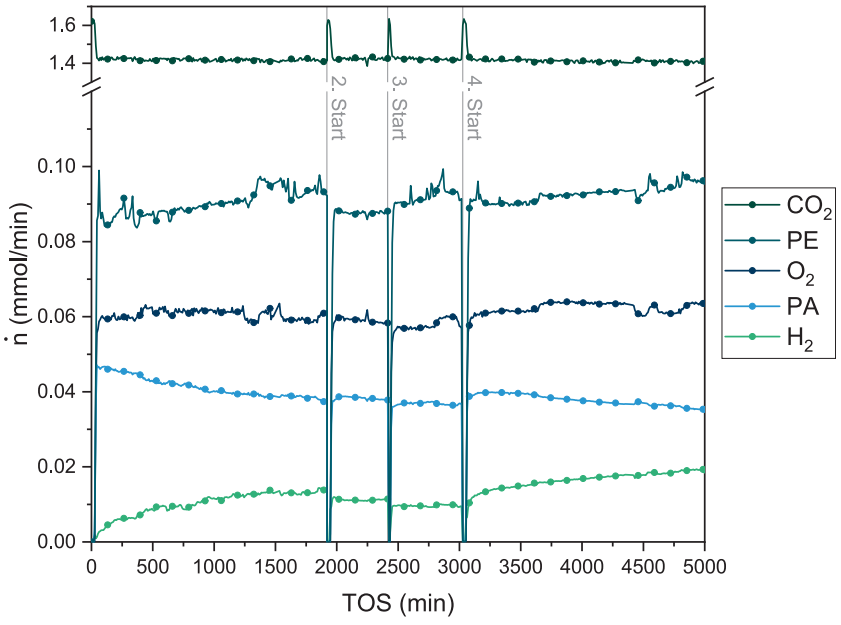

Fig. 15. Gas phase behavior in HyPO with AuPd-TS1-10–1 in four consecutive experiments (runs). Reaction conditions: 0.07 mmol/min H_2, 0.07 mmol/min O_2, 0.14 mmol/min propene, 1.46 mmol/min CO_2; 8 bar, 10C.

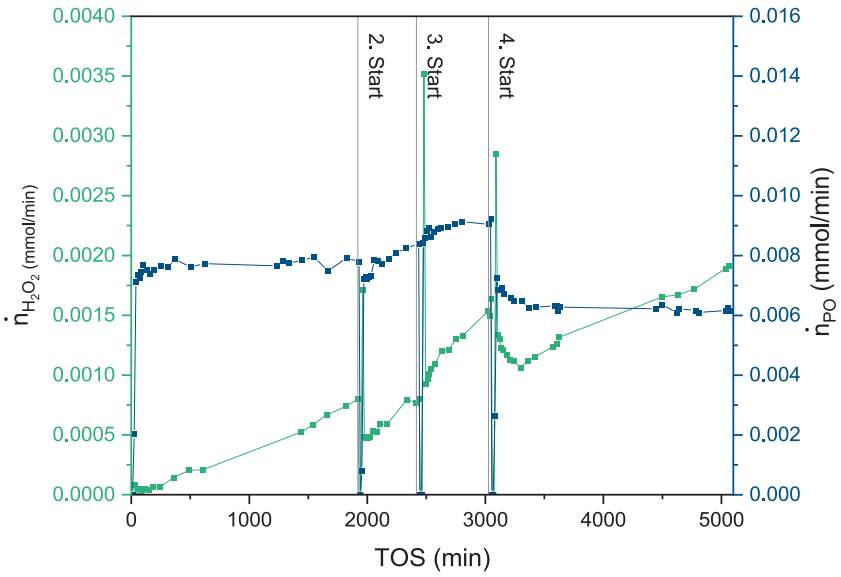

Fig. 16. Production of hydrogen peroxide (green) and propylene oxide (blue) in HyPO with AuPd-TS1-10–1 in four runs. Reaction conditions: 0.07 mmol/min H_2, 0.07 mmol/min O_2, 0.14 mmol/min propene,1.46 mmol/min CO_2; 8 bar, 10C. (For interpretation of the references to colour in this figure legend, the reader is referred to the web version of this article.)

Table 6
Conversion, PO selectivity, hydrogen efficiency and H_2O_2 and PO production rate of HyPO with AuPd-TS1-10-1 in different runs.

Run, TOS	X (H_2) [%]	X (O_2) [%]	X (PE) [%]	S (PO) [%]	HE [%]	P(H_2O_2) [mmol/min]	P(PO) [mmol/min]
1st, 600 min	86.6	9.7	37.8	15.5	12.8	0.0002	0.0077
1st, 1920 min	80.9	11.3	34.8	17.1	14.9	0.0008	0.0078
2nd, 495 min	85.0	23.2	29.7	18.1	14.0	0.0008	0.0084
3rd, 600 min	86.7	17.3	35.6	19.8	17.4	0.0016	0.0091
4th, 600 min	80.0	19.1	27.0	13.9	13.1	0.0017	0.0063
4th, 2005 min	75.4	19.0	24.0	14.8	14.1	0.0019	0.0062

Table 7
Conversion, PO selectivity, hydrogen efficiency and H_2O_2 and PO production rate of HyPO with AuPd-TS1-10-1 in step experiment *DSHP to HyPO* with different reactant ratios (H_2:O_2:PE).

Step, TOS	X (H_2) [%]	X (O_2) [%]	X (PE) [%]	S (PO) [%]	HE [%]	P(H_2O_2) [mmol/min]	P(PO) [mmol/min]
DSHP (1:1:0), 1300 min	99.6	44.7	–	–	26.8	0.0190	–
HyPO (1:1:2), 1500 min	88.9	20.0	34.7	23.5	19.7	0.0013	0.0111
2890 min	83.7	19.9	33.2	22.6	22.2	0.0034	0.0099
HyPO (1:2:1), 3100 min	79.5	23.1	46.8	24.3	26.3	0.0066	0.0083

utilization of the reactants.

3.3.4. Step experiment DSHP to HPPO

In a step experiment, the separated process of DSHP and HPPO were conducted. A H_2O_2 concentration of 0.0165 mmol/ml in MeOH was used for the HPPO, which was taken from the H_2O_2 concentration achieved in the DSHP at 1410 min TOS (Fig. 18). In the switch, the liquid phase was changed from pure methanol to a H_2O_2/MeOH solution and only propene and CO_2 were fed for the HPPO process. In the first phase of the experiment, the DSHP, hydrogen was almost completely converted, as reported in S 14, but a H_2O_2 production rate of only 0.0165 mmol/min was found (Fig. 18), which aligns with the findings of the previous DSHP experiment. With the switch to HPPO process, H_2O_2 was expected to produce an equal amount of propylene oxide, since no side reactions can take place in the absence of hydrogen. Nevertheless, only 70 % PO (0.0115 mmol/min) accounting for the total H_2O_2 feed was obtained even though H_2O_2 was fully converted. At this stage it cannot be explained how the rest of the H_2O_2 is consumed, since the H_2O_2 dismutation can be excluded, according to the results reported in the following section 3.3.5.

3.3.5. H_2O_2 dismutation and hydrogenation

H_2O_2 dismutation was investigated, using a H_2O_2/MeOH solution with a concentration equal to the previous experiment (0.0165 mmol/min). Under an inert CO_2 flow, the system stabilized after 3 h with only 3 % of H_2O_2 decomposition (S 15). The long stabilization might originate from the coordination of H_2O_2 on the titanium sites which are the driving force of the epoxidation mechanism[68]. Overall, the extent of dismutation is minor and can be neglected in the interpretation of the experimental results. After stabilizing the dismutation, hydrogenation of H_2O_2 was investigated in more detail by turning on the H_2 flow (0.07 mmol/min). 40 min after switching, no H_2O_2 was detected, showing that all the fed H_2O_2 was reduced to H_2O, showing that the alloy in AuPd-TS1-10–1 is still highly active in hydrogenation, despite the high gold fraction. In contrast to dismutation, the hydrogenation of H_2O_2 plays a major role in the reaction network.

3.3.6. Hydrogenation of propene

The propene hydrogenation was investigated with AuPd-TS1-10–1. The reaction was conducted with 0.07 mmol/min H_2, 0.14 mmol/min PE, 1.52 mmol/min CO_2, substituting the oxygen flow with CO_2. After 100 min TOS, 97.3 % hydrogen was converted to propane despite the low reaction temperature (S 16) and confirming the high activity of the alloy as in the previous experiment. It needs to be considered that propane production is promoted due to double excess of propene, which

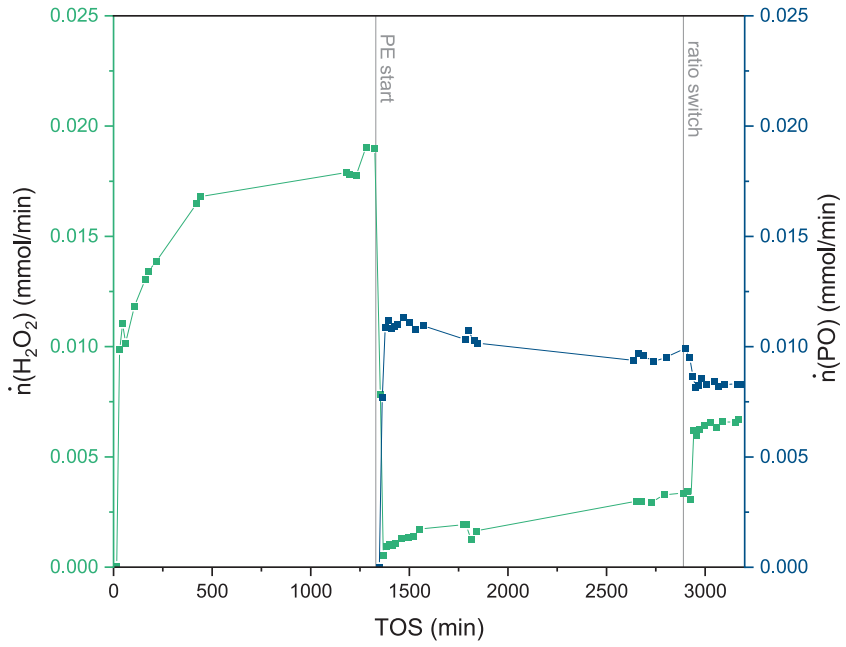

Fig. 17. Production of hydrogen peroxide (green) and propylene oxide (blue) in DSHP and HyPO with AuPd-TS1-10–1. Reaction conditions: first part 0.07 mmol/min H_2, 0.07 mmol/min O_2, 1.60 mmol/min CO_2; second part 0.07 mmol/min H_2, 0.07 mmol/min O_2, 0.14 mmol/min propene, 1.46 mmol/min CO_2; third part 0.07 mmol/min H_2, 0.14 mmol/min O_2, 0.07 mmol/min propene, 1.46 mmol/min CO_2.; in all parts 8 bar, 10C. (For interpretation of the references to colour in this figure legend, the reader is referred to the web version of this article.)

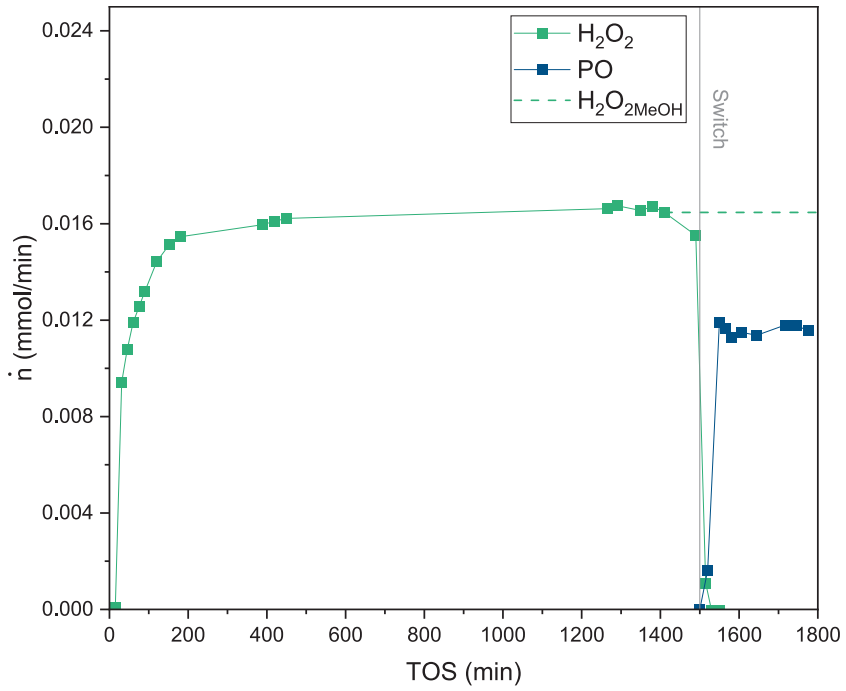

Fig. 18. Production of hydrogen peroxide (green) in DSHP and propylene oxide (blue) in HPPO with AuPd-TS1-10-1 at 8 bar and 10C. Reaction conditions: DSHP 0.07 mmol/min H_2, 0.07 mmol/min O_2, 1.60 mmol/min CO_2; HPPO 0.14 mmol/min propene, 1.60 mmol/min CO_2; 0.0165 mmol/ml H_2O_2 in MeOH. The dashed line is the H_2O_2 concentration used in HPPO. (For interpretation of the references to colour in this figure legend, the reader is referred to the web version of this article.)

was applied in HyPO to shift the chemical equilibrium to PO. It is noteworthy that the hydrogen and propene conversions slightly declined towards the end of the experiment to 93.4 % and 45.1 %, respectively, while the propene conversion was at TOS = 100 min 49.3 %. In conclusion, the experiment shows that the hydrogenation process is a competing reaction to the epoxidation process to a significate extent. Additionally, to the gas analysis, liquid analysis was performed, in which only MeOH and traces of dissolved reactants were detected.

3.3.7. Oxidation of propene

The possibility of propene oxidation was investigated with AuPd-TS1-10–1, where the reaction conditions were maintained as in the

previous experiments and hydrogen was substituted by O_2. Thereby, neither oxygen nor propene were converted, and no oxidation products were detected in the liquid phase analysis.

3.3.8. HyPO with oxygen pre-treatment

As observed in the previous experiments, long-term changes in the activity of H_2O_2 and PO were observed despite several successive and different experiments with the same catalytic bed. It was first assumed that a slow change of the electronic state of the metal nanoparticles might be the reason for this effect. It is known that Pd^{2+} possesses a higher H_2O_2 selectivity than Pd^0, due to the decreased ability of hydrogen activation and subsequent hydrogenation of H_2O_2[10] as well as a higher dissociation energy of the O-O bound[69]. Hence, an experiment with an oxygen pretreatment was performed. Before the actual experiment, another experiment was conducted as a reference under typical reaction conditions for HyPO. After the reference experiment, the catalyst was pretreated with a gas flow rate of 1.25 mmol/min CO_2 and 0.42 mmol/min O_2 at 20°C for 5 h. The same gas flow rates were kept during the catalyst bed wetting with MeOH for 2 h. The production rates of H_2O_2 and propylene oxide in the reference experiment and in the experiment after the oxygen pretreatment were steadily increasing (Fig. 19) as it was observed in the second and third run in HyPO with AuPd-TS1-10–1 (Fig. 16). The final H_2O_2 production rates were 0.0028 mmol/min (reference) and 0.0043 mmol/min (pretreated), while the PO production rates were 0.0098 mmol/min (reference) and 0.0118 mmol/min (pretreated).

Nevertheless, it can be concluded that the pretreatment did not affect the catalyst performance, as the production rates of H_2O_2 and PO continued after the pre-treatment where it has stopped in the reference experiment, as previously observed in other consecutive experiments keeping the catalyst inside the reactor tube. The same trend was observed for the composition of the gas phase, as seen in S 17. It is noteworthy that in the last experiment using AuPd-TS1-10–1, the reaction system was still not stabilized even though the catalyst was used for a total TOS of 184 h, including HyPO, DSHP, HPPO, as well as other tests and additional reactor start up and shut down for each experiment, which are not included in the TOS. This shows a remarkable catalyst stability over time and towards changes in the reaction conditions. In the last experiment, the highest PO production rate was achieved with 0.0118 mmol/min and a PO selectivity of 26.5 % and 25.0 % HE. In contrast, at the end of the third experiment with AuPd-TS1-10–1, the PO production rate was 0.0092 mmol/min with a PO selectivity of 19.8 % and 17.4 % HE (Table 6), confirming the assumption that the efficiency of the reaction system increases with TOS.

3.3.9. HyPO experiments with AuPd-TS1-x-3

In the experiments using catalysts of the third series in HyPO, a similar reaction pattern was observed, in which an increase of the H_2O_2 production rate (S 18) and a decrease of the propane production rate (S 19) were recorded with TOS. Both effects improved the HE and PO selectivity. This trend was found for all the catalysts of the third series as well as in the first HyPO experiment with AuPd-TS1-10-1. AuPd-TS1-10–3 deviated slightly, as a decline in the PO production rate was recorded. However, comparing the first and third catalyst series, the differences in the PO selectivity and HE are outstanding as illustrated in Fig. 20 and reported in S 20. With the catalysts of the third series, PO selectivity in the range of 38.8 – 55.7 % and HE of 28.0 – 33.4 % were achieved, while the experiment with AuPd-TS1-10-1 yielded in a PO selectivity of 16.9 % and 14.6 % HE at TOS = 1500 min.

AuPd-TS1-10–1 produced propane in larger amounts, leading to a decrease of HE and the PO selectivity. The higher H_2 and propene conversion can be related to the smaller size of the AuPd nanoparticles in the catalysts of the first series, that is half of those the third series, resulting in a lower volume-surface ratio. The enhanced accessibility to Pd promotes the Pd-catalyzed hydrogenation of propene and H_2O_2. However, due to the higher active surface, AuPd-TS1-10–1 achieved a PO production rate of 7.9 μmol/min at 1500 min TOS, while the catalysts of the third series yielded only 2.7—3.7 μmol/min. When comparing all catalysts of the third series, a higher H_2O_2 production rate resulted in a higher PO productivity, since more available H_2O_2 can form PO. Thereby, AuPd-TS1-1.5–3 produced the most H_2O_2 and PO. The conversion of propene and oxygen are at a similar level among the catalysts of the third series, while the hydrogen conversion differs from all the catalysts of the third series, with AuPd-TS1-1.5–3 having the highest conversion, followed by AuPd-TS1-5–3 and AuPd-TS1-10–3. The formation of propane can be directly correlated with hydrogen

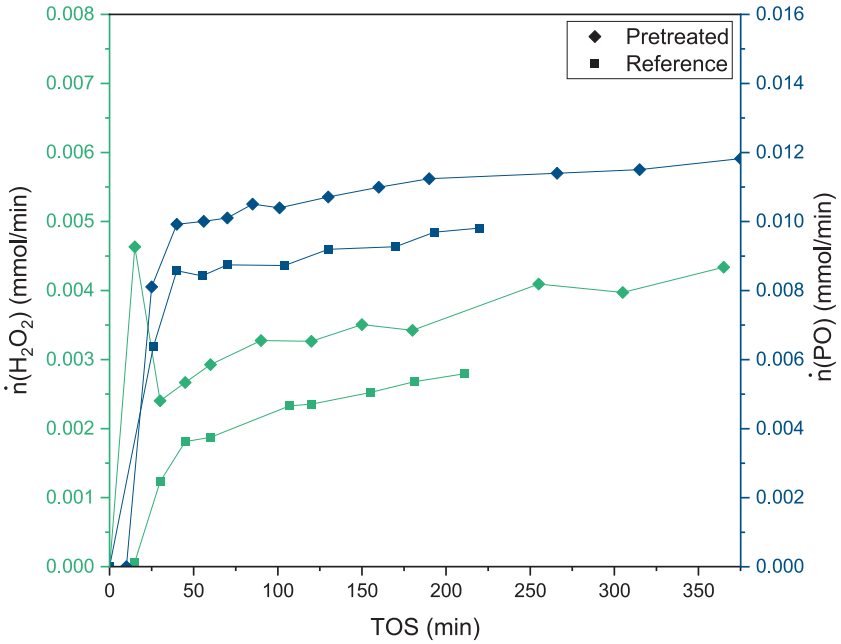

Fig. 19. Production of hydrogen peroxide (green) and propylene oxide (blue) in HyPO using AuPd-TS1-10–1 with oxygen pretreatment (diamond) and without (square). Reaction conditions: 0.07 mmol/min H_2, 0.07 mmol/min O_2, 0.14 mmol/min propene, 1.51 mmol/min CO_2; 8 bar, 10C. (For interpretation of the references to colour in this figure legend, the reader is referred to the web version of this article.)

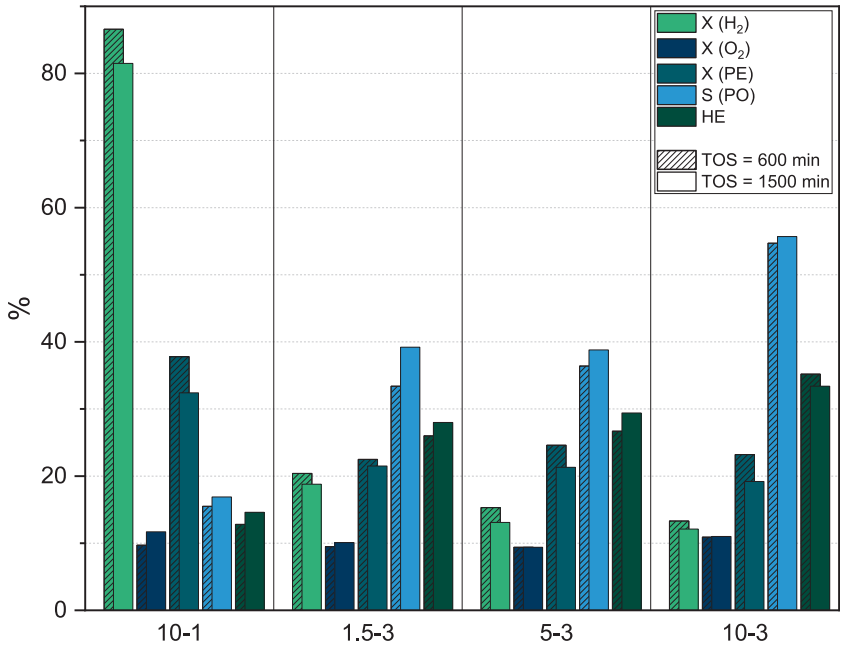

Fig. 20. Comparison of the catalyst performance of AuPd-TS1-10–1 and catalysts of the third series.

conversion, with more converted hydrogen leading to a higher propane production rate. AuPd-TS1-10–3 had the lowest propane production rate, which is mainly the reason for the higher PO selectivity and HE compared to AuPd-TS1-1.5–3 and AuPd-TS1-5–3. Elemental analysis revealed that AuPd-TS1-10–3 has a slightly higher gold content, about 0.015 wt % (Table 8), which could explain the better performance. A correlation between the catalyst performance within the third series and the AuPd particle size was thereby not found (Table 4).

3.4. Catalyst deactivation

To explain long-terms effects in HyPO, the spent catalysts from the reactions were investigated with ICP. The metal loss after all experiments was 4.4 % for AuPd-TS1-1.5–1 and 8.3 % for AuPd-TS1-10–1 (Table 8). The higher metal loss of AuPd-TS1-10–1 is due to the longer TOS, 184 h, while AuPd-TS1-1.5–1 was used for only 31 h. Considering the high TOS, the catalysts were relatively stable. It needs to be noted that the metal content of the spent catalysts can be erroneously reduced due to the contamination of sand from the catalyst bed. The catalysts of the third series had significantly higher metal losses, 23.0 – 32.6 %, compared to AuPd-TS1-10-1 and AuPd-TS1-1.5–1, which affects the H_2O_2 production rates, since the metal is the active phase in the DSHP. In fact, the H_2O_2 production rates were stabilized or declined at TOS = 1500 min using catalysts of the third series while it was steadily increasing using AuPd-TS1-10–1 after the same TOS. The metal composition of the alloy was unchanged in practice for catalyst of the first series with a Pd content from 6.3 – 6.5 % to 6.3 – 6.9 % while for catalysts of the third series it slightly changed from 5.7 – 5.9 % to 2.9 – 3.0 %. The stability of the alloy was underlined by STEM-EDS line scans of the spent AuPd-TS1-10–1 and AuPd-TS1-10–3, in which Au and Pd occurs at the same locations, as reported in S 21and S 22.

Table 8
Metal loading fresh and spent catalysts, after HyPO, percentage metal loss and Pd content in alloy of fresh and spent catalysts.

Catalyst	Metal content (Au/ Pd) wt% fresh	Metal content (Au/ Pd) wt% spent	Δ metal (Au/Pd) [a] %	Pd in AuPd fresh/ spent %
AuPd-TS1-1.5-1	0.365 (0.342/ 0.024)	0.349 (0.327/ 0.022)	4.3 (4.2/6.2)	6.5/6.3
AuPd-TS1-10-1	0.366 (0.343/ 0.023)	0.336 (0.313/ 0.023)	8.3 (8.8/0.1)	6.3/6.9
AuPd-TS1-1.5-3	0.383 (0.360/ 0.023)	0.271 (0.263/ 0.008)	29.3 (27.1/ 65.2)	5.9/2.9
AuPd-TS1-5-3	0.382 (0.359/ 0.022)	0.294 (0.285/ 0.009)	23.0 (20.6/ 61.4)	5.9/2.9
AuPd-TS1-10-3	0.398 (0.375/ 0.023)	0.268 (0.260/ 0.008)	32.6 (30.7/ 64.2)	5.7/3.0

[a] percentage loss of total metal, total Au and Pd between fresh and spent catalyst.

The differences in the metal loss of the different catalyst series can be explained by the SEM analysis in Fig. 21 of the spent catalysts, confirming the significant removal of the metal aggregates after the reaction. Since in AuPd-TS1-1.5–1 and AuPd-TS1-10–1 much less metal aggregates were found than in the catalysts from the third series (Fig. 6), the metal loss of the catalyst is expected to be low and this was confirmed by ICP analysis of the spent catalysts. The anatase impurity is a fortunate circumstance as the agglomeration of AuPd was reduced with a higher anatase content and a strong metal-support-interaction is provided, seen in the charge transfer, Fig. 12, and a reduced acidity of the metal modified TS-1 materials was obtained (Table 5).

In Fig. 22, the comparison of AuPd nanoparticle sizes of the catalysts before and after HyPO reaction is illustrated. The AuPd nanoparticles of AuPd-TS1-10–1 show a significant increase in their mean size of 1.9 nm on anatase, while the increase in AuPd-TS1-1.5–1 is only 1.4 nm on anatase. In the third catalyst series, the size of AuPd nanoparticles on anatase in AuPd-TS1-1.5–3 is unchanged, while in AuPd-TS1-5–3 and AuPd-TS1-10–3 they increased 1.9 nm and 2.5 nm, respectively. Only AuPd-TS1-1.5–3 achieved in HyPO a stable PO production rate within the catalysts of the third series (S 18). AuPd on TS-1 only increased significantly in AuPd-TS1-10–1 and AuPd-TS1-5–3, whereas in other catalysts an interpretation of the particle size change is difficult, considering the measurement error. Besides this finding, no other pattern was found that could be correlated with the results of the catalytic experiments. The increase of the AuPd nanoparticles affects the catalytic performance, particularly in the DSHP step of HyPO, since less active surface is available. However, the metal loss is likely the dominating reason for the catalyst deactivation, since the H_2O_2 activity increased for AuPd-TS1-10–1 despite the increased metal nanoparticle

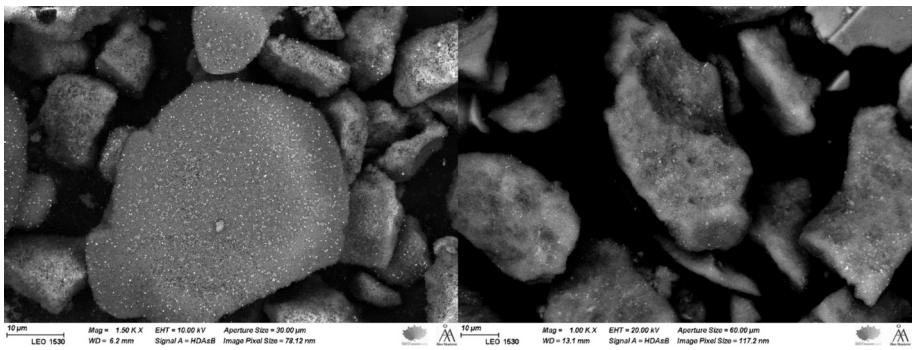

Fig. 21. SEM images of AuPd-TS1-10–3 fresh (left) and spent (right), after HyPO reaction.

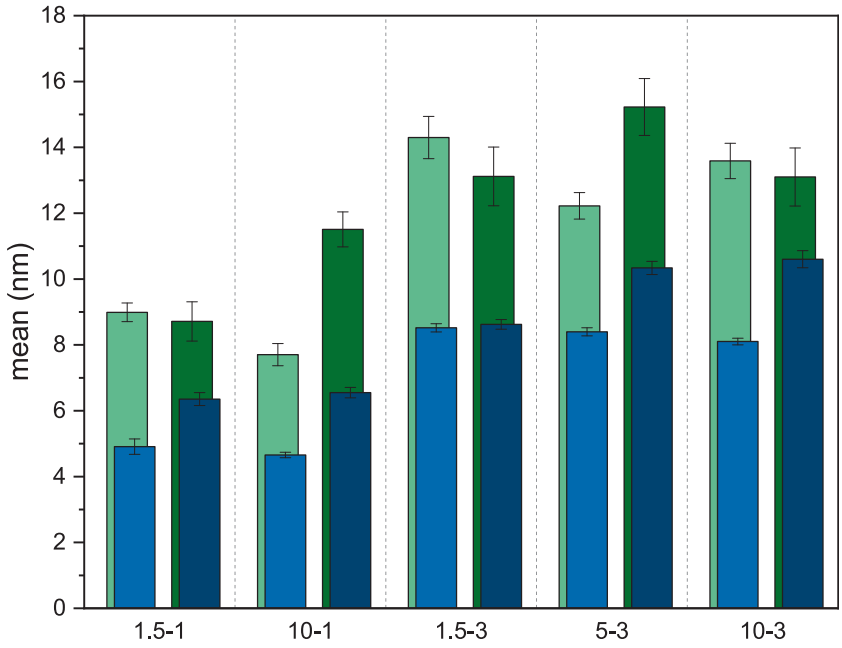

Fig. 22. Mean sizes of AuPd on TS-1 (green) and anatase (blue) of different AuPd-TS1-x-x catalysts. Fresh catalysts are indicated bright and spent dark. (For interpretation of the references to colour in this figure legend, the reader is referred to the web version of this article.)

size.

The spent catalysts AuPd-TS1-10–1 and AuPd-TS1-10–3 were characterized using XPS (Fig. 12). The loss of the intensities of the Au and Pd peaks is the most prominent change in the spectra compared to the fresh catalysts, reflected in a higher signal-to-noise ratio for the fresh sample. The intensity loss is higher for AuPd-TS1-10–3 compared to AuPd-TS1-10–1, confirming the leaching results. In AuPd-TS1-10-1, the Au^{1+} content of gold remained practically unchanged being 28 % and 25 % in the fresh and spent materials, respectively. In general, the oxidation state of the metals was found unaltered even though a change was expected because of the long-term changes in the catalytic performance. However, it cannot be ruled out that *in-situ* reduced metal had been partially re-oxidized outside the reactor. In the Ti spectra, the peak position of the framework Ti shifted from 360.4 eV to 359.4 eV in AuPd-TS1-10–1 while for AuPd-TS1-10–3 the peak was only partially shifted. During the reaction in HyPO, the coordination of the tetrahedral Ti changed due to H_2O and H_2O_2 to a $Ti(OSi)_2(OH)_2(H_2O)_2$ environment, leading to a lower BE[70].

Further examination of the spent catalysts was conducted with thermogravimetric analysis to investigate if higher polyglycol species were absorbed at the catalyst surface, which could occur in HPPO[71] causing blockages of active sites. An indication of carbon species was provided by the XPS spectra of the spent catalysts (S 23), in which a carbon peak increased after the reaction in HyPO increased, corresponding to a C-O bonding[72]. Nevertheless, the thermogravimetric analysis showed after the water loss no further mass changes and thus the adsorption of this kind of compounds is not considered as a reason for the catalyst deactivation.

4. Conclusions and outlook

The present work reports for the first time continuous epoxidation of propene with *in-situ* generated hydrogen peroxide in liquid phase under mild conditions of 8 bar and 10°C. The process to develop a TS-1 AuPd bimetallic supported catalyst for this reaction system, active both in direct synthesis of hydrogen peroxide and in propene epoxidation, was described. These catalysts include the metal sites able to activate hydrogen in the formation of H_2O_2 with only a moderate olefin hydrogenation due to a Pd-poor alloy, together with the Ti sites that perform the epoxidation with the in-situ generated hydrogen peroxide. The synthesized catalysts were extensively characterized to evaluate the synthetic method and their properties. It was demonstrated how the catalyst preparation is affected and even benefits from the anatase impurities present in the commercial TS-1, due to the higher capability to anchor the metal precursors on the metal deposition step.

The synthesized and characterized catalysts were successfully tested

in HyPO. A PO selectivity up to 55.7 % and hydrogen efficiency of up to 33.4 % were achieved. In addition, the properties of the spent catalysts were investigated to elucidate the deactivation observed during the experiments. Furthermore, the development and optimization of the HyPO process was discussed. The first important results of this research shed light on the complex dynamics of the continuous process, for instance the increase of the PO selectivity and HE with TOS, and demonstrated the benefits of combining both processes, e.g. suppression of hydrogenation of H_2O_2 during the HyPO process due to the competing coverage of the olefin on the metal nanoparticles.

Nevertheless, further experiments and characterizations are needed to obtain a deeper understanding of the reaction network. Process intensification can potentially be achieved by varying the metal composition and the catalyst loading and the pre-treatment of the catalytic materials as well as by varying the catalyst bed structure and reaction conditions.

CRediT authorship contribution statement

Christoph Schmidt: Writing – original draft, Visualization, Validation, Software, Methodology, Investigation, Formal analysis, Data curation, Conceptualization. **Matias Alvear:** Writing – original draft, Validation, Methodology, Investigation, Conceptualization. **Francesco Sandri:** Writing – original draft, Visualization, Validation, Methodology, Investigation, Formal analysis, Conceptualization. **Seo Mandon:** Visualization, Validation, Methodology, Investigation, Data curation. **Satu Ojala:** Writing – original draft, Supervision, Methodology, Investigation, Formal analysis, Conceptualization. **Tiina Laitinen:** Writing – original draft, Visualization, Validation, Methodology, Investigation, Formal analysis, Data curation. **Mika Lastusaari:** Writing – original draft, Visualization, Validation, Methodology, Investigation, Conceptualization. **Ilari Angervo:** Writing – original draft, Visualization, Validation, Methodology, Investigation, Data curation, Conceptualization. **Tapio Salmi:** Visualization, Validation, Supervision, Resources, Project administration, Methodology, Investigation, Funding acquisition, Formal analysis, Conceptualization.

Declaration of competing interest

The authors declare that they have no known competing financial interests or personal relationships that could have appeared to influence the work reported in this paper.

Acknowledgments

This work is part of the activities of Johan Gadolin Process Chemistry Centre (PCC) at Åbo Akademi. The research has been financed by Academy of Finland, through the Academy Professor grants 319002 and 320115 (T.S. and C.S.), the Scholarship of the Rector of Åbo Akademi and Neste and Fortum Foundation (C.S.). Part of the work was carried out with the support of the Centre for Material Analysis, University of Oulu, Finland.

Appendix A. Supplementary data

Supplementary data to this article can be found online at https://doi.org/10.1016/j.jcat.2025.116637.

Data availability

Data will be made available on request.

References

[1] S. Fukuzumi, Y. Yamada, K.D. Karlin, Electrochim. Acta 82 (2012) 493–511.
[2] R. Ciriminna, L. Albanese, F. Meneguzzo, M. Pagliaro, ChemSusChem 9 (2016) 3374–3381.
[3] A. Goti, F. Cardona, In: P. Tundo, V. Esposito (Eds.), Springer Netherlands, Dordrecht, 2008, pp. 191–212.
[4] J.M. Campos-Martin, G. Blanco-Brieva, J.L.G. Fierro, Angew. Chemie Int. Ed. 45 (2006) 6962–6984.
[5] R.J. Lewis, G.J. Hutchings, ChemCatChem 11 (2019) 298–308.
[6] P. Biasi, P. Canu, F. Pinna, T. Salmi, *Chem. Eng. Trans.* **2011**, *24*, 49-54 SE-Research Articles.
[7] T. Nyman, Safety Study of Hydrogen Peroxide Direct Synthesis, Lappeenranta University of Technology, 2013.
[8] F. Ni, T. Richards, L.R. Smith, D.J. Morgan, T.E. Davies, R.J. Lewis, G.J. Hutchings, ACS Org. Inorg. Au 3 (2023) 177–183.
[9] G. Sharp, R.J. Lewis, J. Liu, G. Magri, D.J. Morgan, T.E. Davies, Á. López-Martín, R.-J. Li, C.R. Morris, D.M. Murphy, et al., ACS Catal. 14 (2024) 15279–15293.
[10] C. Samanta, Appl. Catal. A. Gen. 350 (2008) 133–149.
[11] H. Xu, D. Cheng, Y. Gao, ACS Catal. 7 (2017) 2164–2170.
[12] S.J. Freakley, Q. He, J.H. Harrhy, L. Lu, D.A. Crole, D.J. Morgan, E.N. Ntainjua, J. K. Edwards, A.F. Carley, A.Y. Borisevich, et al., Science (80-) 351 (2016) 965–968.
[13] J.C. Pritchard, Q. He, E.N. Ntainjua, M. Piccinini, J.K. Edwards, A.A. Herzing, A. F. Carley, J.A. Moulijn, C.J. Kiely, G.J. Hutchings, Green Chem. 12 (2010) 915–921.
[14] J.K. Edwards, S.J. Freakley, A.F. Carley, C.J. Kiely, G.J. Hutchings, Acc. Chem. Res. 47 (2014) 845–854.
[15] R. Todorovic, R.J. Meyer, Catal. Today 160 (2011) 242–248.
[16] V.R. Choudhary, C. Samanta, T.V. Choudhary, Appl. Catal. A. Gen. 308 (2006) 128–133.
[17] J. Brehm, R.J. Lewis, D.J. Morgan, T.E. Davies, G.J. Hutchings, Catal. Letters 152 (2022) 254–262.
[18] P. Biasi, N. Gemo, J.R. Hernández Carucci, K. Eränen, P. Canu, T.O. Salmi, Ind. Eng. Chem. Res. 51 (2012) 8903–8912.
[19] F. Frison, C. Dalla Valle, C. Evangelisti, P. Centomo, M. Zecca, Catalysts 9 (2019) 10.3390/catal9020124.
[20] G. Li, J. Edwards, A.F. Carley, G.J. Hutchings, Catal. Today 122 (2007) 361–364.
[21] M. Taramasso, G. Perego, B. Notari, Preparation of Porous Crystalline Synthetic Material Comprised of Silicon and Titanium Oxides, **1983**, US4410501A.
[22] R.J. Lewis, K. Ueura, Y. Fukuta, T.E. Davies, D.J. Morgan, C.B. Paris, J. Singleton, J. K. Edwards, S.J. Freakley, Y. Yamamoto, et al., Green Chem. 24 (2022) 9496–9507.
[23] A.J.H.P. van der Pol, J.H.C. van Hooff, Appl. Catal. A. Gen. 106 (1993) 97–113.
[24] S.C. Laha, R. Kumar, J. Catal. 208 (2002) 339–344.
[25] Research Nester, "Propylene Oxide Market," can be found under https://www.researchnester.com/reports/propylene-oxide-market/2804, **2024**.
[26] T.A. Nijhuis, M. Makkee, J.A. Moulijn, B.M. Weckhuysen, Ind. Eng. Chem. Res. 45 (2006) 3447–3459.
[27] V.-H. Nguyen, B.-S. Nguyen, C. Hu, A. Sharma, D.-V.-N. Vo, Z. Jin, M. Shokouhimehr, H.W. Jang, S.Y. Kim, Q.V. Le, Catalysts (2020) 10, https://doi.org/10.3390/catal10040442.
[28] F. Song, Y. Liu, L. Wang, H. Zhang, M. He, P. Wu, in From Zeolites to Porous MOF Mater. - 40th Anniv. Int. Zeolite Conf. (Eds.: R. Xu, Z. Gao, J. Chen, W.B.T.-S. in S.S. and C. Yan), Elsevier, **2007**, pp. 1236–1243.
[29] X. Liu, X. Wang, X. Guo, G. Li, Catal. Today 93–95 (2004) 505–509.
[30] M. Alvear, F. Orabona, K. Eränen, J. Lehtonen, S. Rautiainen, M. Di Serio, V. Russo, T. Salmi, Chem. Eng. Sci. 269 (2023) 118467.
[31] T. Hayashi, K. Tanaka, M. Haruta, J. Catal. 178 (1998) 566–575.
[32] Z. Li, Z. Su, W. Ma, Q. Zhong, Appl. Catal. A. Gen. 615 (2021) 118060.
[33] X. Feng, Z. Song, Y. Liu, X. Chen, X. Jin, W. Yan, C. Yang, J. Luo, X. Zhou, D. Chen, ACS Catal. 8 (2018) 10649–10657.
[34] Q. Chen, E. Beckman, Green Chem. - Green Chem. (2008) 10, https://doi.org/10.1039/b803847c.
[35] J. Su, J. Zhou, C. Liu, X. Wang, H. Guo, Chinese J. Catal. 31 (2010) 1195–1199.
[36] L. Lutterotti, Nucl. Instruments Methods Phys. Res. Sect. B Beam Interact. with Mater. Atoms **2010**, 268, 334–340.
[37] R.H. Perry, D.W. Green, Perry's Chemical Engineers' Handbook, McGraw-Hill International Edition, 1997.
[38] F. Sandri, M. Danieli, M. Zecca, P. Centomo, ChemCatChem 13 (2021) 2653–2663.
[39] Z.K. Lopez-Castillo, S.N.V.K. Aki, M.A. Stadtherr, J.F. Brennecke, Ind. Eng. Chem. Res. 47 (2008) 570–576.
[40] J. De Laat, G. Truong Le, B. Legube, Chemosphere 55 (2004) 715–723.
[41] P. Biasi, J. García-Serna, A. Bittante, T. Salmi, Green Chem. 15 (2013) 2502–2513.
[42] M. Alvear, K. Eränen, D.Y. Murzin, T. Salmi, Ind. Eng. Chem. Res. 60 (2021) 2430–2438.
[43] A. Santos, R.J. Lewis, G. Malta, A.G.R. Howe, D.J. Morgan, E. Hampton, P. Gaskin, G.J. Hutchings, Ind. Eng. Chem. Res. 58 (2019) 12623–12631.
[44] N. Yap, R.P. Andres, W.N. Delgass, J. Catal. 226 (2004) 156–170.
[45] R. Zanella, S. Giorgio, C.R. Henry, C. Louis, J. Phys. Chem. B 106 (2002) 7634–7642.
[46] L. Delannoy, S. Giorgio, J.G. Mattei, C.R. Henry, N. El Kolli, C. Méthivier, C. Louis, ChemCatChem 5 (2013) 2707–2716.
[47] S. Ivanova, C. Petit, V. Pitchon, Appl. Catal. A. Gen. 267 (2004) 191–201.
[48] T. Dong, Q. Huang, L. Chen, J. Peng, H. Hu, Q. Huang, X. Chen, Chem. Phys. Lett. 804 (2022) 139880.
[49] A. Wróblewska, J. Grzeszczak, P. Miądlicki, K. Kiełbasa, M. Kujbida, A. Kamińska, B. Michalkiewicz, Materials (basel) 14 (2021), https://doi.org/10.3390/ma14247799.
[50] M. Shamzhy, B. Gil, M. Opanasenko, W.J. Roth, J. Čejka, ACS Catal. 11 (2021) 2366–2396.

[51] C. Lamberti, S. Bordiga, A. Zecchina, A. Carati, A.N. Fitch, G. Artioli, G. Petrini, M. Salvalaggio, G.L. Marra, J. Catal. 183 (1999) 222–231.
[52] D.L. Liao, G.S. Wu, B.Q. Liao, Colloid. Surf. A Physicochem. Eng. Asp. 348 (2009) 270–275.
[53] A.M. Joshi, W.N. Delgass, K.T. Thomson, J. Phys. Chem. B 110 (2006) 16439–16451.
[54] A. Venäläinen, K. Meinander, M. Räisänen, V. Tuboltsev, J. Räisänen, Surf. Sci. 677 (2018) 68–77.
[55] J. Radnik, C. Mohr, P. Claus, Phys. Chem. Chem. Phys. 5 (2003) 172–177.
[56] N. Kruse, S. Chenakin, Appl. Catal. A. Gen. 391 (2011) 367–376.
[57] Y.G. Li, Y.M. Lee, J.F. Porter, J. Mater. Sci. 37 (2002) 1959–1965.
[58] D. Brassard, M.A. El Khakani, L. Ouellet, J. Appl. Phys. 102 (2007) 34106.
[59] P. Ratnasamy, D. Srinivas, H. B. T.-A. In: C. Knözinger (Ed.), Academic Press, **2004**, pp. 1–169.
[60] J. Sun, Z. Zhang, E. Yang, W. Du, F. Liu, K. Xu, Y. Zhong, X. Duan, X. Zhou, Nano Res. 17 (2024) 7182–7193.
[61] ACS Materials LLC, "TS-1 Molecular Sieve," can be found under https://www.acsmaterial.com/blog-detail/ts-1-molecular-sieve.html?srsltid=AfmBOopcpJpE21QQerGnTLNyLF20rRMyJGAua1wLrW8I0-F78bUH7Hxq, **2018**.
[62] J. Lu, X. Zhang, J.J. Bravo-Suárez, T. Fujitani, S.T. Oyama, Catal. Today 147 (2009) 186–195.
[63] J. Su, G. Xiong, J. Zhou, W. Liu, D. Zhou, G. Wang, X. Wang, H. Guo, J. Catal. 288 (2012) 1–7.
[64] P. Biasi, F. Menegazzo, F. Pinna, K. Eränen, P. Canu, T.O. Salmi, Ind. Eng. Chem. Res. 49 (2010) 10627–10632.
[65] Messergroup, "Propene," can be found under chrome-extension://efaidnbmnnnibpcajpcglclefindmkaj/https://www.messergroup.com/documents/921887/0/Propen+%281%29.pdf/12b5a54b-bbcd-579e-f183-56adca90ae4e?t=1681909315872, **n.d.**
[66] O. Reinsdorf, K. Eränen, T. Salmi, Catalysts (2023) 13, https://doi.org/10.3390/catal13040753.
[67] C.P. Gordon, H. Engler, A.S. Tragl, M. Plodinec, T. Lunkenbein, A. Berkessel, J. H. Teles, A.-N. Parvulescu, C. Copéret, Nature 586 (2020) 708–713.
[68] P.E. Sinclair, C.R.A. Catlow, J. Phys. Chem. B 103 (1999) 1084–1095.
[69] F. Wang, C. Xia, S.P. de Visser, Y. Wang, J. Am. Chem. Soc. 141 (2019) 901–910.
[70] L. Wu, X. Deng, S. Zhao, H. Yin, Z. Zhuo, X. Fang, Y. Liu, M. He, Chem. Commun. 52 (2016) 8679–8682.
[71] Q. Wang, L. Wang, J. Chen, Y. Wu, Z. Mi, J. Mol. Catal. A Chem. 273 (2007) 73–80.
[72] G. Greczynski, L. Hultman, Sci. Rep. 11 (2021) 11195.